Ionospheric Disturbances During Magnetic Storms at SANAE

A thesis submitted in fulfilment of the

requirements for the degree of

MASTER OF SCIENCE

of

RHODES UNIVERSITY

Department of Physics and Electronics at Rhodes University

by

Alicreance HIYADUTUJE

September 2016

Abstract

The coronal mass ejections (CMEs) and solar flares associated with extreme solar activity may strike the Earth's magnetosphere and give rise to geomagnetic storms. During geomagnetic storms, the polar plasma dynamics may influence the middle and low-latitude ionosphere via travelling ionospheric disturbances (TIDs). These are wave-like electron density disturbances caused by atmospheric gravity waves propagating in the ionosphere. TIDs focus and defocus SuperDARN signals producing a characteristic pattern of ground backscattered power (Samson *et al.*, 1989). Geomagnetic storms may cause a decrease of total electron content (TEC), i.e. a negative storm effect, or/and an increase of TEC, i.e. a positive storm effect. The aim of this project was to investigate the ionospheric response to strong storms (Dst < -100 nT) between 2011 and 2015, using TEC and scintillation measurements derived from GPS receivers as well as SuperDARN power, Doppler velocity and convection maps. In this study the ionosphere's response to geomagnetic storms is determined by the magnitude and time of occurrence of the geomagnetic storm. The ionospheric TEC results of this study show that most of the storm effects observed were a combination of both negative and positive per storm per station (77.8%), and only 8.9% and 13.3% of effects on TEC were negative and positive respectively. The highest number of storm effects occurred in autumn (36.4%), while 31.6%, 28.4% and 3.6% occurred in winter, spring and summer respectively. During the storms studied, 71.4% had phase scintillation in the range of 0.7 - 1 radians, and only 14.3% of the storms had amplitude scintillations near 0.4. The storms studied at SANAE station generated TIDs with periods of less than an hour and amplitudes in the range 0.2 - 5 TECU. These TIDs were found to originate from the high-velocity plasma flows, some of which are visible in SuperDARN convection maps. Early studies concluded that likely sources of these disturbances correspond to ionospheric current surges (Bristow *et al.*, 1994) in the dayside auroral zone (Huang *et al.*, 1998).

Acknowledgement

Dedication

I dedicate this thesis to my wife, Uwineza, my sons, Hiyadutuje and Hiyadutije, my brothers, Hiyaduhaye and Hiyaduhanze, my sisters, Hiyadukunze and Hiyadutunze and to my late parents, Hungulimana and Ntakaziraho.

Contents

List of Figures

List of Tables

Chapter 1

Introduction

1.1   Introduction

The ionosphere in the polar regions is closely connected to the space environment through the Earth's magnetic field, and exhibits complex plasma dynamics (Feldstein and Levitin, 1986). These dynamics can be further complicated by sudden or large energy and particle injections during geomagnetic storms. The response of the polar ionosphere to the geomagnetic storm is of interest because the ionospheric manifestation of these responses can severely affect radio communication (Davies, 1990a; Hargreaves, 1992). It is also important to understand these sudden and large dynamic changes, as they can extend to middle and lower ionosphere through the thermospheric winds, which affect the global chemical composition. Also during strong geomagnetic storms the magnetospheric convection electric fields which play an important role in plasma redistribution at polar regions can extend to lower latitudes and cause various effects at these latitudes (Foster and Rich, 1998; Kikuchi *et al.*, 2000; Thomas *et al.*, 2013). Energy input from the solar wind and/or magnetosphere into the polar region during magnetic storms can launch atmospheric gravity waves which manifest as large scale travelling ionospheric disturbances (LSTIDs) in the ionosphere (Huang *et al.*, 2000). These LSTIDs may also cause dynamic changes to the ionosphere.

The response of the ionosphere to geomagnetic storms depends on the nature of the storm, i.e. the intensity and/or the duration of the storm. One of the responses of the ionosphere to energy injection associated with magnetic storms is the generation of TIDs which may be seen as plasma perturbations over a short duration of time (De Abreu *et al.*, 2010a; Ding *et al.*, 2013). These TIDs also might be associated with atmospheric gravity waves and/or

Joule heating. These TIDs are observed to focus and defocus the Super Dual Auroral Radar Network (SuperDARN) ground-backscattered signals and are manifested in power, Doppler velocity and spectral width (Hunsucker, 1982; Samson *et al.*, 1989; Hayashi *et al.*, 2010; Karpachev *et al.*, 2010; Grocott *et al.*, 2013; Oinats *et al.*, 2015). It is very important to study the response of the ionosphere to geomagnetic storms because these disturbances play an important role in the dynamics of the thermosphere; for example, TIDs propagate in the ionosphere and help us to understand the global energy redistribution, as well as the variation of total electron content (TEC) (Hayashi *et al.*, 2010; Idrus *et al.*, 2013). TEC is the total number of electrons in the field of view (FOV) of a receiver to the satellite, contained in an imaginary cylinder of the cross-section of 1 m^2 (El-Rabbany, 2002). The TEC is measured in TEC unit (TECU), such that 1 TECU = $10^{16} m^{-2}$.

Geomagnetic storms may have a positive (i.e. increase of electrons) or negative (decrease of electrons) effect on the ionosphere, with the atomic and molecular composition of the thermosphere playing an important role in determining which of these effects will occur. This contributes to knowledge of the vertical motion of the ionosphere (Tsagouri *et al.*, 2000; De Abreu *et al.*, 2010b). When a radio signal (RS) passes through the ionosphere, the amplitude and phase of this signal are sometimes affected and give rise to amplitude and/or phase scintillations (Dubey *et al.*, 2006). Scintillations are due to multiple paths of a signal after passing through ionospheric irregularities and suffers both refraction and diffraction. Strong scintillation may disturb the propagation of radio signals through the ionosphere. The satellite-based communication and navigation systems may be affected (Dubey *et al.*, 2006; Idrus *et al.*, 2013).

The study of ionospheric scintillation aids in understanding the formation and localisation of ionospheric irregularities with their consequent effects on communication and technology (Basu *et al.*, 1983).

1.2   Objective of the research

The polar ionospheric regions differ from lower latitude regions, because of the divergence and convergence of both open and closed geomagnetic field lines at the southern and northern polar regions, respectively. In these regions, during geomagnetic storms, solar wind particles infiltrate the Earth's upper atmosphere, resulting in immense precipitation of charged (energetic) particles travelling along disturbed magnetic field lines, as well as energy deposition. These particles change the ionospheric plasma density and result in ionospheric irregularities (Pi *et al.*, 1997). Disturbance Storm Time (Dst) indices are included in this study to show the geomagnetic activities of the selected days. The Auroral Electrojet (AE) indices also are included in this study to show the current intensity which results in Joule heating during these storm days (De Jesus *et al.*, 2016). During geomagnetic storms, geomagnetic field indices may decrease or increase according to the severity of the storms (Table 2.1) (Loewe and Prölss, 1997). This research investigates the nature of ionospheric disturbances associated with geomagnetic storms, by means of GPS, TEC and scintillation measurements, in conjunction with SuperDARN HF radar measurements obtained from Antarctic base stations.

This research studies the response of the ionosphere to geomagnetic storm in order to understand plasma motion which may be associated with observed ionospheric disturbances during these storms. GPS TEC, GPS scintillation, SuperDARN's SANAE site's relative power and Doppler velocity from ground scatter and SuperDARN convection map measurements were used. Seven days were chosen with the storm day in the middle, in order to investigate responses of thirteen strong geomagnetic storms and one severe storm between 2011 and 2015. The main objectives of the project were to:

- Categorise the effects of the geomagnetic storms as positive, negative, or a combination of (negative and positive),

- Investigate and characterise scintillation during geomagnetic storms,

- Determine the characteristics of TIDs launched by geomagnetic storms,

- Investigate the driving mechanisms of the ionospheric storm effects and the observed TIDs as well as their source regions.

1.3 Brief overview of chapters

The dissertation is divided into five chapters:

- Chapter 1 introduces, motivates and expresses the objective of the research.

- Chapter 2 contains the theoretical background needed to understand the ionosphere and its morphology, geomagnetic storms and their characteristics and impact of geomagnetic storms on the ionosphere.

- Chapter 3 describes the methodology for obtaining and using GPS data, SuperDARN data and other measurements.

- Chapter 4 gives and explains ionospheric responses found during geomagnetic storms, using GPS TEC, scintillation and SuperDARN measurements at SANAE and other GPS stations in Antarctica.

- Chapter 5 summarises the conclusions of this study.

Chapter 2

Theoretical background

2.1 The Earth's ionosphere

The ionosphere is an ionised region consisting of electrons and ions around the Earth, located at an altitude of ~ 50 km to ~ 1000 km. It is a natural resource that is exploited for high-frequency (HF) radio applications due to its properties that contribute to the reflection of HF radio signals. The ionosphere is created by extreme ultraviolet (EUV) radiations from the Sun due to the interaction of photons with neutral atoms to generate free electrons. Electrons in the outer shells of atoms are energised by EUV radiation and become disassociated from their original atom, resulting in free electrons and positively charged ions. This process is called photo-ionisation. Concurrent to this process is the recombination process where the electrons are lost when they recombine with positively charged ions to produce neutral atoms. However, the rate of recombination is a slow process thus free electrons always exist in the ionosphere, especially in the higher altitude F-region of the ionosphere. The reverse process is known as recombination, which restores the neutral atoms and reduces the number of free electrons. Satellite and rocket measurements show that oxygen atoms O are the main neutral species in F_2-region. However, the rate of recombination is a slow process thus free electrons always exist in the ionosphere. The O^+ is expected to be the most prevalent ion, due by photoionisation according to the following equation:

$$O + h\nu \rightarrow O^+ + e^- \tag{2.1}$$

where h is the Planck constant, ν is the frequency given by c/λ , $h\nu$ is the photon energy, c is the speed of light in a vacuum and λ is the wavelength.

2.1.1 The regions of ionosphere

At altitudes above the F-region peak ($\sim$ 200 - 350 km) ionisation is not significant even though there is strong radiation, because the atmosphere is thin (i.e. it has fewer neutral particles). At lower altitudes, even though the gas for ionisation is abundant, the EUV is not strong due to the loss of energy from absorption at higher altitudes; therefore, again ionisation is low. At certain altitudes, the EUV is strong enough and there are sufficient species to ionise, therefore there is maximum ionisation. During the day the ionosphere has four regions, namely the D, E, F_1 and F_2 regions, because at different altitudes different atoms dominate and these absorb EUV energy at different wavelengths (McNamara, 1991).

- The D region starts at $\sim$ 50 and ends at $\sim$ 90 km above the Earth's surface. It has an electron density of the order of $10^2 - 10^3$ cm^{-3} (as shown in Figure 2.1) and the density of the neutral atmosphere is of the order of $10^{14} cm^{-3}$. The D region has metal ions such as Ca^+, Fe^+, Na^+ and hydrated ions such as H_3O^+, $H_5O_2^+$, $H^+(H_2O)_n$ and others. In this region, NO is ionised by solar X-rays or Lyman alpha and the electron attachment to O and O_2 forms negative ions. During recombination, electrons form negative ions which are destroyed by photodetachment during the daytime, associative detachment ($O + O^- \rightarrow O_2 + e^-$.), and mutual neutralisation (for A a neutral atom, $O^- + A^+ \rightarrow O + A$) (Leadon et $al.$, 1981; McNamara, 1991; Savage and Sembach, 1996; Kelley, 2009).

- The E region starts at $\sim$ 90 and ends at $\sim$ 150 km above the Earth's surface. It has an electron density of the order of $10^3 - 10^5$ cm^{-3} (as shown in Figure 2.1). In this region, O, O_2, and N_2 are ionised by absorption of energy from EUV radiation and solar X-rays. Dominant ions are O^+, N^+ and NO^+. The dissociative recombinations ($O_2^+ + e \rightarrow O + O$) and ($NO^+ + e \rightarrow N + O$) take place in this region (Leadon et $al.$, 1981; McNamara, 1991; Savage and Sembach, 1996; Kelley, 2009).

- The F_1 region is located at $\sim$ 150 to $\sim$ 200 km above the Earth's surface. It has an electron density of the order of $10^5 - 10^6$ cm^{-3} (as shown in Figure 2.1). O and N_2 are the dominant species and are ionised by Lyman (continuum) and after sunset, the ionisation of N_2 disappears. Most of the ionisation is in molecular form and disappears by dissociative recombination (Leadon et $al.$, 1981; McNamara, 1991; Savage and

Sembach, 1996; Kelley, 2009).

- The F_2 region is located above F_1, from ~ 200 km above the Earth's surface. It has
  an electron density of the order of $10^5 - 10^6$ cm^{-3} (as shown in Figure 2.1) and the
  density of the neutral atmosphere of the order of $10^8 cm^{-3}$. The effective recombination
  rate decreases as the ionospheric height increases, thus this region has more ions than
  others. Molecular recombination is similar to that of the F_1 layer, by means of an
  attachment-like recombination law for charge transfer (Leadon $et\ al.$, 1981; McNamara,
  1991; Savage and Sembach, 1996; Kelley, 2009).
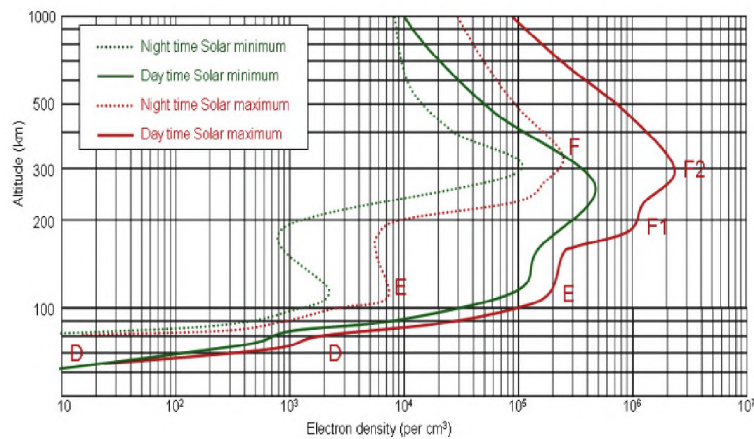
Figure 2.1: The ionospheric regions and electron density (Loudet, 2016).

2.1.2   Variation of the ionosphere

The ionospheric electron density (plasma) varies with latitude, day to day, seasons and solar
activity.

1. Latitudinal variation: The ionosphere has distinct features at different latitude:

   - The equatorial (low) latitudes are situated below 20° geomagnetic latitudes: The
     north-south geomagnetic field lines are almost horizontal. The equatorial ionisa-
     tion anomaly (EIA) is located in the F_2-region at these latitudes. The EIA is
     characterised by a dense trough of electrons at the magnetic dip equator and a
     dual band of increased electron density at about 15° north and south of the trough.
     It is associated with the eastward electric field during the day. The plasma is lifted

to higher altitudes by $\mathbf{E} \times \mathbf{B}$ and pressure gradient against the gravitational force, which then diffuses downward along the field lines into both hemispheres. This is known as the fountain effect (Stolle *et al.*, 2008).

- The middle latitude is, situated between 20° and 60° geomagnetic latitudes: This region is mostly controlled by the balance between photoionisation and recombination. However, thermospheric winds also significantly contribute to the vertical motion of the ions and electrons in this region. The ions move more or less in the same direction as the wind while the electrons move nearly at right angles. The magnetic field gives rise to the Lorentz force, but the collision of the particles and neutral gases gives rise to a drag force in this region. The ions and electrons are forced to flow in the direction of the wind, which give rise to differential motion between them due to the Lorentz force and electric current. The region in which this wind strongly encourages the generation of the electric current is called the dynamo region. The electric current and neutral winds cause the upward/downward movement of plasma driven by electric fields or winds, resulting in ionospheric enhancements/depletions of electron density at the mid-latitudes. In the F_2-region, the plasma moves along the magnetic field lines to higher altitudes around sunrise (Hargreaves, 1995; Hunsucker and Hargreaves, 2007). In the evening the protons flow back to lower levels in order to maintain this region of the ionosphere (Salah and Holt, 1974; Hargreaves, 1992).

- The high latitudes are situated around 60° geomagnetic latitudes and higher: In these regions the geomagnetic field is almost vertical relative to the Earth's surface. The charged particles from the Sun spiral around the lines of force of the Earth's magnetic field. The structure of this field allows these particles to penetrate the lower level of the ionosphere. They collide with components of the neutral atmosphere and cause the collisional ionisation process. The electron density in the high-latitude ionosphere depends on the solar zenith angle and on the particles arriving into the region from the Sun. At E region (about 100 km), the important feature called the auroral oval is produced by the process of collisional ionisation. The energy transported by the high-speed charged particles manifests itself as visible light (aurora) during collisions with the atoms of the neutral atmosphere.

The auroral oval expands and contracts with changes in the solar wind. During quiet conditions, this region contracts to a narrow band of a few degrees wide and expands equatorward during disturbed conditions (Yizengaw *et al.*, 2005). As one moves towards the poles out of the tropical zone between the Tropics of Cancer and Capricorn, the zenith angle increases and reduces the photoionisation there (McNamara, 1991; Chavalier, 2007).

This region exhibits large variation in ion composition, concentration and temperature that cause variability in the source, loss, and transport of plasma. The convective flow of plasma perpendicular to the magnetic field contributes to the plasma and the energy loss rates. The superposition of a typical polar electric field distribution and the corotation of electric field gives a steady convection pattern. In the evening sector, the steady flow of the wind blows the ionisation along the magnetic field based on the fact that the electrons are not free to move horizontally (they are confined by the Earth's magnetic field). The northerly wind blows ionisation down the magnetic field line to lower altitudes where the ionisation is more quickly destroyed. In the polar cap region, a tongue of ionisation may be formed by the high-density plasma convection. In high latitudes, the neutral winds and $\mathbf{E} \times \mathbf{B}$ drifts cause the upward and downward motions (drifts) of the ionosphere. During strong disturbance conditions, the convection pattern expands and the drift speeds increase. This causes the formation of new troughs and density enhancements, changing the plasma distribution in the polar ionosphere (Prölss, 1995). An accurate measurement of convection is done by considering the $\mathbf{E} \times \mathbf{B}$ drift velocity of irregularities in the ionospheric F_2-region. The transmitted signals of SuperDARN are coherently backscattered by these irregularities.

2. Diurnal variation: At first approximation, the diurnal variation may be described by the level of the maximum production rate of free electrons as a function of solar zenith angle. For a simplified case where the optical depth (τ) is constant;

$$q_m = q_0 cos\chi$$

where χ is the solar zenith angle.

$$q_0 = \frac{I_\infty \sigma_i}{e H \sigma_a}$$

where I_∞ is the radiation intensity outside the atmosphere, and where σ_a and σ_i are the absorption cross-section for the atomic (molecular) species and the partial cross-section of ionisation, respectively. $e \simeq 2.71828$, q_m is the peak production rate of the ion-electron pairs per unit volume per second, and H is the scale height. τ is dimensionless and is a measure of how far into the atmosphere the radiation has penetrated, measured in terms of the attenuation the radiation has suffered. At midday, the level of ionisation is higher, because the solar zenith angle is approximately zero. At sunset, the level of ionisation is very low, because the solar zenith angle is approximately 90°. When recombination takes place, there is a reduction of free electrons. The ionosphere's electron density increases during the day and decreases during the night (Figure 2.1) (Chavalier, 2007; McNamara, 1991). The D and F_1 regions appear during the day and tend to disappear completely at night. The E region appears during the day and sometimes also at night. The F_2 region appears during the day and during the night for the whole year.

3. Seasonal variation: The neutral atmosphere (atomic or molecular) and the solar zenith angle also varies from season to season, which means that the level of ionisation varies with season. The level of ionisation in summer is higher than the level of ionisation in winter because the zenith angle at noon is always greater than the corresponding zenith angle in summer (Chavalier, 2007; McNamara, 1991). When the Earth's southern hemisphere has winter or autumn, the Earth's northern hemisphere has summer or spring season and vice versa. The reason for this permutation of seasons is due to the position of the Sun relative to the Earth's rotation axis.

4. Solar cycle variation: The solar cycle spans ~ 11 years. The number of sunspots indicates how active the Sun is, such that during high solar activity the number of sunspots is at a maximum and during low solar activity the sunspot number is at a minimum. The monthly median values of electron density are linearly related to the monthly average value of the number of sunspots such that the minimum number (i.e.

low solar cycle), corresponds to low electron densities and the maximum number (i.e. high solar cycle), corresponds to high electron densities (Chavalier, 2007; McNamara, 1991).

2.1.3   Radio wave absorption in the ionosphere

A radio wave carries energy in its motion and when it encounters an electron in its trajectory, its energy is absorbed by the electron. The electron then vibrates or oscillates at the same frequency as the wave. The same electron looses the same energy in the form of a radio wave. This transfer of energy continues to the next electron and so on, until the radio wave reaches its destination. There is no absorption, if the intensity, the frequency, the amplitude and the power of a wave remain the same. Otherwise part of the energy or all the energy is lost through absorption. Absorption happens when the electron, which absorbs the radio wave energy, collides with a heavy neutral atom, because the atom doesn't vibrate or oscillate at the same frequency as that of the radio wave, due to its mass, and so the atom uses the energy to increase its speed. In the ionosphere from the D- to F_2-regions, the neutral atomic density decreases, therefore there is more absorption in the D-region compared to the F_2-region. Radio waves are better absorbed during the day than during the night because the D-region disappears at night (Figure 2.1). Radio waves are also significantly absorbed at higher levels of solar activity due to enhancement of electron density. The absorption also depends on the polarisation of a radio wave. Within the ionosphere electrons gyrate or move around the magnetic fields when there are no collisions. The electric field of circularly polarised waves, may increase or slow down the speed of the electrons. If the electrons absorb more energy, they increase their radii around the magnetic field and this increases the probability of collision with the neutral atoms and they loose their energy. It has been found that extraordinary waves (X-waves) increase the speed of electrons, while ordinary waves (O-waves) decrease their speed. This means that X-waves are better absorbed than O-waves and they may be completely absorbed when their frequency is equal to the frequency of the electron gyrating around magnetic field line. This results in a total absorption of a such wave (McNamara, 1991).

2.1.4   Irregularities and scintillation in the ionosphere

The ionospheric irregularities are small-scale structures in the ionospheric plasma. They follow the magnetic field lines and cause field-aligned irregularities (FAIs) after being stretched out along the lines of force. The reason is that the electrons (in irregular form) can move around the field lines, but not across them. When there are FAIs, a single pulse reflected by the ionosphere will be spread or stretched in time, with echoes arriving with time delays longer than those normally observed (McNamara, 1991). The scale length of ionospheric irregularities may range from a few meters to several kilometers across the magnetic field. Most of the time they occur in the auroral and polar cap F_2-region. Ionospheric irregularities are increased by geomagnetic storms and may be generated artificially by radio wave heating experiments.

During a geomagnetic storm, the formation of the storm-enhanced density and the ionospheric trough caused by energetic particle precipitation were found to be related with the mid- and high-latitudes GPS phase irregularities. Different irregularities within the polar cap regions were found to be related with storm-enhanced density/tongue of ionization and the polar patches (Cherniak *et al.*, 2015). In this thesis, the parameters for the study of scintillations are the amplitude and the phase of a received signal. Amplitude scintillations affect signal fades and enhancements due to the destructive and constructive interferences of radio wavefronts passing through irregularities. These events lead us to GPS errors of decoding data and ranges calibration (Davies, 1990b; Carrano *et al.*, 2005). Due to the ionospheric irregularities, phase fluctuations may cause the degradation of a radio signal leading to the loss of signal lock which need for navigation signals (Yizengaw *et al.*, 2005). If a planar radio wave hits a number of irregularities, it suffers random phase fluctuations across the wavefront. The wave is refracted and/or diffracted and therefore the wave signal reaches the receiver through multiple paths (Carrano *et al.*, 2005; Sreeja *et al.*, 2011). When combining the phase scintillation and amplitude measurements, one can determine the integrated electron density deviation, the geometry of the propagation and anisotropy of irregularities (Bernhardt *et al.*, 2006). Analyzing variability of the spectra shape, the decorrelation time, the cumulative distributions functions of signal amplitude, the fade durations, the distributions of phase and amplitude rates and the depolarization effects from scattering of equatorial anomaly region

data, one can investigate the effects of scintillations on HF radio communication and radar system (Basu *et al.*, 1983).

2.2 Earth's magnetic field

The outer core of the solid Earth has magma which generates convection currents, by means of the dynamo mechanism. The heat flow from the inner core creates electric currents by the Coriolis force, hence the Earth's magnetic field (Buffett, 2000; Sakuraba and Roberts, 2009). The geomagnetic field shields the Earth's lower atmosphere from the impact of the solar wind and cosmic rays. The inner part of the Earth's magnetic field may be compared to a bar magnet of which the southern end is pointed at around 79° S and 110° E, and northern end is pointed 79° N and 70° W. The geomagnetic latitude and longitude are measured in the same way as the geographic latitude and longitude. The strength of the geomagnetic field is measured by considering the electron gyro-frequency. The charged particles gyrate and
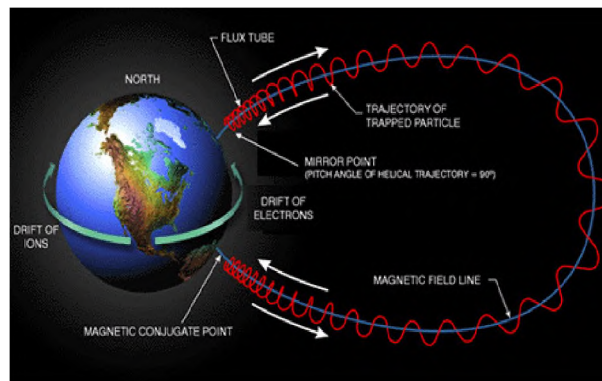
Figure 2.2: Charged particles in the geomagnetic field (Jursa *et al.*, 1985).

bounce between magnetic mirrors, ions drift westward and electrons drift eastward (Figure 2.2). The drift is an effect of the gradient and curvature of the dipole magnetic field and is oppositely directed for ions and electrons. The magnetic mirror is a static magnetic field that, within a localised region, has a shape such that approaching charged particles (such as electrons) are bounced back along their path of approach. For a particular angle called the pitch angle, those particles are trapped and stay in these three motions in the geomagnetic field (Chen Francis, 1974). Other particles are lost in the loss cone due to their small pitch angles caused by higher collision frequencies, and collide with atmospheric neutral atoms and ions (Esposito, 2003).

The components of the geomagnetic field at the surface of the Earth are described as follows (Figure 2.3): X is the northward geographic component, Y is the eastward geographic component and Z is the vertical component. The horizontal intensity (H) is given by:

$$H = \sqrt{X^2 + Y^2} \tag{2.2}$$

The total intensity (F_2) is given by:

$$F = \sqrt{X^2 + Y^2 + Z^2} \tag{2.3}$$

The dip (inclination) angle (I) is given by:

$$I = \arctan\left(\frac{Z}{H}\right) \tag{2.4}$$

and the declination angle D is given by:

$$D = \arctan\left(\frac{Y}{X}\right) \tag{2.5}$$

The intensity of the magnetic field is usually measured in nano-Tesla (nT $= 10^{-9}$ T). It is stronger at the poles than at the equator. It also reduces as one moves far from the Earth's surface to the upper atmosphere (Campbell, 2003).
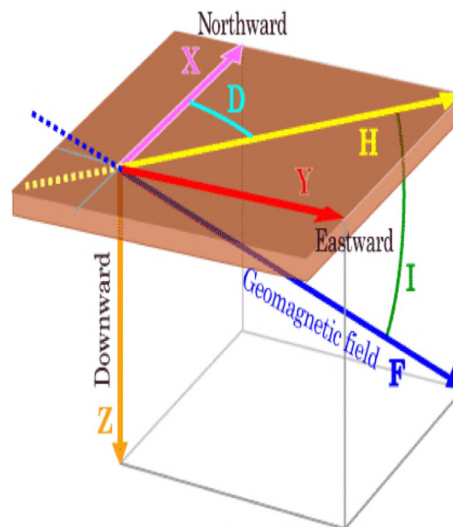
Figure 2.3: Elements of the geomagnetic field (Kyoto, 2016).

2.3   Geomagnetic storms

During a geomagnetic storm the Earth's magnetic field is disturbed by shocks from solar wind energy injections, solar coronal mass ejections (CMEs), solar flares and by interaction with interplanetary magnetic field (IMF) (Axford, 1962; Gonzalez *et al.*, 1994; Danilov and Lastovicka, 2001; Chavalier, 2007). When the vertical component of the IMF and the Earth's magnetic fields are oppositely directed, they create the neutral points and the Earth's magnetic field lines break down and result in a connection between the IMF and geomagnetic field lines, as shown in Figure 2.4 (Gonzalez *et al.*, 1994). The connection allows the flow of magnetic and particle energy into the Earth's magnetosphere to create geomagnetic storms and substorms (Gonzalez *et al.*, 1994; Walker, 2004). The Earth's ring current is an electric
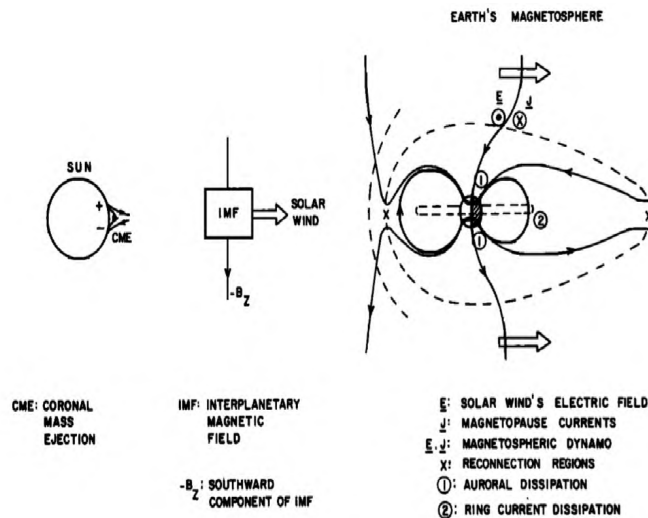
Figure 2.4: Geomagnetic reconnection (Gonzalez *et al.*, 1994).

current due to the longitudinal drift of charged particles, with energy between 10 to 200 keV in the Earth's magnetosphere during this period. These particles generate a magnetic field in a direction opposite to the geomagnetic field in the inner side and reduce an observed magnetic field in this region. During a geomagnetic storm, the number of energetic particles in the ring current increases and strongly reduces the geomagnetic field (Kennel, 1996).

The measurement of the severity of a geomagnetic storm is done by using Dst index, which is the measure of the reduction of the horizontal components of the Earth's magnetic field. Geomagnetic storms are classified by their effect on the ionosphere. Table 2.1 shows differ-

ent classes of geomagnetic storms based on their minimum Dst and the median of auroral electrojet (AE-med) indices. A geomagnetic storm has 3 phases:

Table 2.1: Different classes of the geomagnetic storms (Loewe and Prölss, 1997).

Geomagnetic storm class	Range of minimum Dst index (nT)	AE-med index (nT)
Weak	-30 to -50	542
Moderate	-50 to -100	728
Strong	-100 to -200	849
Severe	-200 to -350	1017
Great	$\leq$ (less than or equal to) -350	1335

1. Initial phase (IP): During this phase, there is a rapid increase in the geomagnetic field or its measurement (Dst), caused by the stream of protons and electrons, brought for a few minutes, by the solar wind. These hit the Earth's magnetopause resulting in Sudden Commencement (SC) or Sudden Storm Commencements (SSC). This is part of an initial or a positive phase which can last for a few hours leading to an increase in the geomagnetic field (Dst) (see Figure 2.5).

2. Main phase (MP): This phase starts when the H component of magnetic field at the equator decreases due to the westward ring current around the Earth. The particles with different energies/species don't arrive near the Earth at the same time because they have different velocities. This phase may last some hours. The decrease in the density of the stream causes a decrease in Dst until it reaches its minimum value (see Figure 2.5).

3. Recovery phase (RP): During this phase, the IMF turns north and the ring current decays to gradually increase the Earth's magnetic field. The Dst slowly returns to the quiet time value and this phase lasts for several hours or a few days (see Figure 2.5) (Ferraro, 1952).

2.3.1   Negative storm effects in the ionosphere

A rapid expansion of polar ionisation enhancement caused by an increased input of energy at high-latitudes causes an upwelling of the neutral atmosphere and decreases the atom-to-molecule ratio as the air of different composition (with less light atoms/molecules) is raised
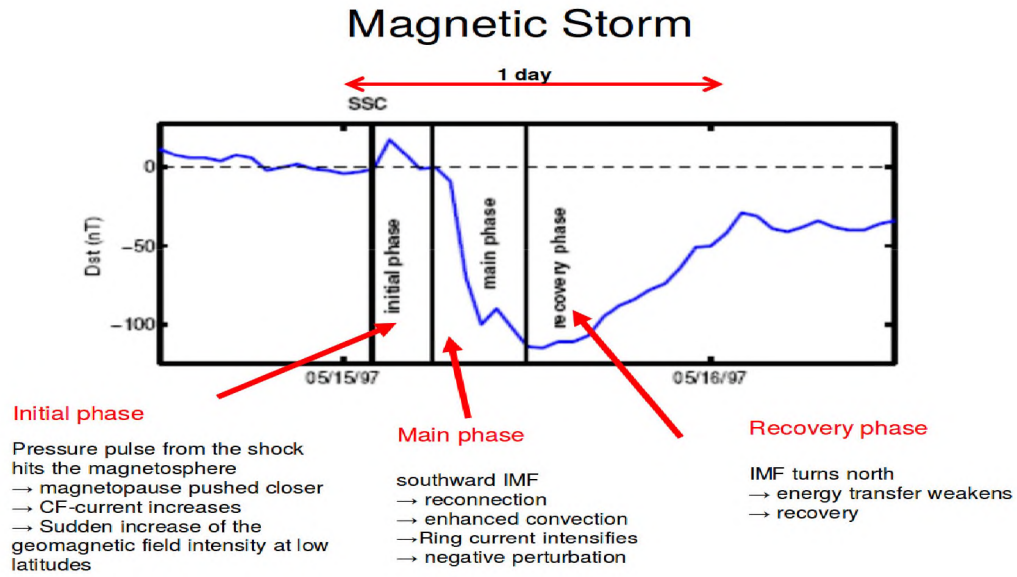
Figure 2.5: The geomagnetic storm phases (Lakhina and Tsurutani, 2011).

to high altitudes. A rapid heating and expansion of the atmosphere at high latitudes causes a pressure gradient, which in turn, modifies the global thermospheric circulation and gives rise to enhanced equatorward winds. The recombination increases in the ionosphere and reduces electron density because of this change in chemical composition. For example, depletion of oxygen and enhancement of the molecular nitrogen densities play a very important role in the ionospheric study during geomagnetic storms because they reduce the ionisation density at the F_2-region altitudes. The production of ionisation at the F_2-region altitude is based on photoionisation of atomic oxygen in (equation 2.1). On the assumption that the atmosphere is optically thin, the production rate (q) is directly proportional to the atomic oxygen density ($[O]$) (Prölss, 1995).

$$q = J_o[O] \tag{2.6}$$

where J_o is the ionisation frequency of this constituents. The loss of ionisation at the F_2-region altitude is caused by the charge transfer reactions of the following type

$$O^+ + N_2 \xrightarrow{k_1} NO^+ + N \tag{2.7}$$

$$O^+ + O_2 \xrightarrow{k_2} O_2^+ + O \tag{2.8}$$

where k_1 and k_2 are the associated reaction rate constants. The resulting molecular ions NO^+ and O_2^+ are destroyed by dissociative recombination. The loss rate can be written as

$$l(N) = \beta[O] \tag{2.9}$$

where N is electron density, β depends on the density of the molecular gases N_2 and O_2.

$$\beta = k_1[N_2] + k_2[O_2] \tag{2.10}$$

The measured composition changes are used to identify the storm effects by calculating the ratio of the disturbed to the undisturbed value of O and N_2. The ratio $R(n)$ is the storm-time value of the gas constituent n divided by the respective quiet-time value.

$$R(N_m) \simeq \frac{R(O)}{R(N_2)} = R\left(\frac{O}{N_2}\right) \tag{2.11}$$

where N_m is the maximum electron density and is given by

$$N_m = \frac{q}{\beta} \tag{2.12}$$

An increase in N_2 density and a decrease in the O density implies a decrease in $\frac{[O]}{[N_2]}$ which results in a decrease in the electron density, because a repeating decrease of the density of O leads to the reduction of the ionisation production rate.

The electric fields are responsible for the transport of electrons and the increase of the loss of ionisation. The reason is that there are strong correlations between the reaction rate of the constants k_1 and k_2 (in equation 2.10) and both the ion temperature and the relative flow speeds of the interacting gases. At high latitude, k_1 is proportional to the square of the effective temperature. This effective temperature increases roughly with the square of the effective electric field strength by means of electrodynamic heating. The chemical loss rates affect the plasma density, where any chemical change (not driven by dynamics) is the production of vibrationally excited molecular nitrogen. These species increase the plasma loss coefficient and the enhanced loss rate will result in significant decreases in the F_2-region electron density (Fuller-Rowell *et al.*, 1994). The increase of the loss rate creates veritable holes in

the plasma density and the formation of new troughs both at sub- and transauroral latitudes.

During geomagnetic storms, Joule heating causes a strong upwelling of the atmosphere around the auroral oval and leads to a variety of dynamic and chemical changes in the atmosphere. Particle precipitation is a very important source of ionisation in the polar ionosphere, especially during solar eclipse and winter solstice conditions. During strong disturbance conditions, particle precipitation leads to density enhancement at the higher latitudes (Prölss, 1995). The Joule heating and electrodynamic drift are associated with the auroral electrojets (Figure 2.6). During a geomagnetic storm, Joule heating can reach 50.0% of the total energy input into the ionosphere. This energy input is the manifestation of the Ohmic interaction of some currents and the electric field in the ionosphere.
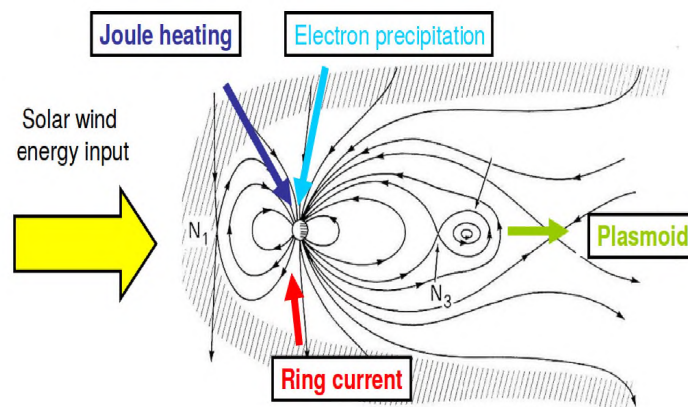
Figure 2.6: The Joule heating, the electron precipitation and the ring current in the ionosphere (Kamide and Baumjohann, 1993; Stern, 1996).

The mean molecular mass is increased in the upwelling region (due to convergence winds) and decreased in the downwelling region, and its increase causes the negative storms at higher latitudes. Upwelling and increases in molecular oxygen tend to hasten the ion recombination and cause a decrease in plasma density (Fuller-Rowell *et al.*, 1994). During a geomagnetic storm, enhanced Joule heating at high latitudes decreases the normal poleward wind on the dayside and reinforces the regular equatorward wind on the nightside and creates a storm circulation that can transport air with increased molecular species. This increase in the

molecular species results in an increased recombination of O^+ and a decrease in the electron density in F_2-region (Huang *et al.*, 2005; Burns *et al.*, 2007).

The particle precipitation causes thermal expansion and large upward flows which amplify the decrease in the ionisation density. The perturbations caused by neutral composition changes are applicable to the polar regions (as shown in Figure 2.7). The auroral energetic particle precipitation also causes negative storm effects when the auroral oval shifts towards the equator during a geomagnetic storm (Danilov and Lastovicka, 2001). This is due to the fact that very little of the energy in the form of energetic particle precipitation (kinetic energy) flows around the auroral oval, while the most of the energy is associated with the cross-polar cap potential drop. The dissipation of energy occurs in the area of the auroral oval and its effects may be considered as a source of heating around the auroral oval. During the evening sector, the auroral oval shifts toward the equator, where the ion convection pattern can cause flux tubes to remain for a considerable time in a region where recombination occurs but production doesn't (Fuller-Rowell *et al.*, 1994; Danilov and Lastovicka, 2001; Burns *et al.*, 2007). Ionisation depletion in F_2-region is also caused by the increased recombination rate due to ion-neutral frictional heating caused by the rapid ion flows through the dayside convection during polar cap expansion (Yizengaw *et al.*, 2005).

2.3.2   Positive storm effects in the ionosphere

Obayashi and Matuura (1972) suggested that positive ionospheric storms are also caused by neutral composition changes. For severely disturbed conditions, no evidence has been reported to support this supposition (Prölss, 1995; Burns *et al.*, 2007). By contrast, the idea that positive ionospheric storms are caused by the transport of ionisation is well supported by observations (Prölss, 1995; Burns *et al.*, 2007). The high latitude heat input increases the meridional pressure gradient and enhances the global circulation of winds. Winds blow ions up field lines into regions where the recombination is slower, hence enhancing the electron concentration (Fuller-Rowell *et al.*, 1994; Burns *et al.*, 2007). At high latitudes, the neutral composition through wind circulation pulls the molecular-species-rich air upwards, increasing the density of the molecular species compared to atomic species and hence the ratio of recombination to production at the F_2 peak (Burns *et al.*, 2007). Huang et al. (2005) suggested

that the enhanced eastward electric field played an important role in the generation of the observed positive storm phase at middle latitudes. The electric field moves the F_2-region plasma to higher altitudes, resulting in increases in the F_2-region electron density. During storms or substorms, an enhanced convection electric field moves nightside plasmaspheric plasma from higher to lower L-shells with smaller volumes, which increases the plasma pressure in the magnetic flux tube and downward plasma fluxes. These fluxes are one sources of the enhancement of electron density in the F_2-region. Another cause of the density increase in polar latitudes is an uplifting of the F_2-region due to the energy injections (the energy injections are shown in Figure 2.7) (Prölss, 1995; Tsagouri *et al.*, 2000; Lu *et al.*, 2001; Horvath, 2007; De Abreu *et al.*, 2010b; Horvath and Lovell, 2015). It was found that $\frac{[O]}{[N_2]}$ increases
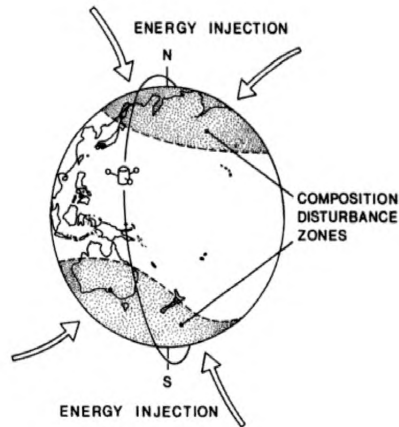
Figure 2.7: The polar energy deposition and the composition disturbance zones (Prölss, 1995).

with height and the increase in this ratio means the increase in electron density. Mikhailov *et al.* (1995) and Lu *et al.* (2001) suggested that positive storm effects may also be caused by travelling atmospheric disturbances (TADs) by uplifting the F_2-region. The uplifting of the F_2-region of ionosphere leads to less recombination rate, which results in the increase of the plasma density.

2.3.3   Travelling ionospheric disturbances

Travelling ionospheric disturbances (TIDs) are wave-like of electron density disturbances caused by atmospheric gravity waves (AGWs) propagating in the ionosphere. These disturbances are divided into two main classes: large-scale traveling ionospheric disturbances

(LSTIDs) and medium-scale travelling ionospheric disturbances (MSTIDs). LSTIDs have horizontal wavelengths of more than 1000 km and periods of between 30 min and 3 hours, and MSTIDs have horizontal wavelengths of several hundreds of kilometers and period between 15 min and 1 hour (Hocke and Schlegel, 1996; Hayashi *et al.*, 2010; Grocott *et al.*, 2013; Oinats *et al.*, 2015). Medium scale TIDs are the most common phenomema while large scale TIDs are mostly associated with geomagnetic storms. During geomagnetic storms large scale TIDs are generated in the auroral or sub-auroral region, as a result of Lorentz forces and Joule heating caused by the enhancement of auroral electrojets and/or intense precipitation of charged particles (Waldock and Jones, 1986; McHarg *et al.*, 2005; Palmroth *et al.*, 2005; Ding *et al.*, 2008). Storm-induced TIDs mostly propagate from higher latitudes towards mid- and low-latitudes and sometimes cross the equator poleward (Tsugawa *et al.*, 2004; Ding *et al.*, 2008; Habarulema *et al.*, 2015). However, recently Habarulema et al. (2015) reported LSTIDs travelling poleward at 730 ± 78 m/s velocity, generated by the equatorial electrojet during a geomagnetic storm period over the African sector. TIDs can be measured using instruments such as ionosonde, incoherent scatter radar, HF Doppler, GPS, and airglow imager. The studies of LSTIDs using GPS Earth observation network (GEONET) and international GNSS service (IGS) in Japan and Australia showed independent of LSTIDs and electromagnetic waves. LSTIDs and electromagnetic waves in northern and southern hemispheres were dependent on AGWs and propagated equatorward (Idrus *et al.*, 2013).

2.4   Summary

The formation of the ionosphere, its morphology and the different conditions which may cause changes in its behaviour, were explained. Temporal, spatial and geophysical modifications of the ionosphere were discussed. Radio wave propagation and its attenuation were described. Geomagnetic storms and their effects on the ionosphere were also detailed. The third chapter focuses on obtaining GPS TEC, GPS scintillation and SuperDARN HF radar data. Conditions for the selection of selecting the used data are discussed and explanations of data processing methods are given.

Chapter 3

Data and method

The global positioning system (GPS) consists of 30 satellites and its primary use is to determine the position and velocity of a fixed or moving object, located over or near the Earth's surface. GPS operates at L-band radio frequencies of 1227.6 and 1575.42 MHz and therefore used to study the ionosphere as these frequencies are affected by the free electrons in this layer. GPS observes irregularities between meter-and hectometer-scales (Basu *et al.*, 1996; Otsuka *et al.*, 2006). Super Dual Auroral Radar Network (SuperDARN) is an international collaborative network of high frequency radars for investigating the Earth's upper atmosphere and ionospheric plasma irregularities. SuperDARN operates within the frequency range 8–20 MHz, and can detect irregularities at decameter-scale, i.e. $\sim$ 10s m (Greenwald *et al.*, 2006). These instruments have been used to investigate ionospheric disturbances and irregularities of various scale, for example TID characteristics (Yizengaw, 2004; Kaplan and Hegarty, 2005; Kantor *et al.*, 2006; NASA, 2016).

In this study, GPS and SuperDARN HF radars were selected to investigate the response of ionosphere during strong storms since GPS gives information on the state of the ionosphere through TEC measurement and SuperDARN gives information on ionospheric irregularities and plasma flow through power and Doppler velocity measurements, as well as convection maps. Also phase and amplitude scintillation measurements were obtained from GPS data for the scintillation characterization study. Dst and AE indices were used as indicators of the magnitude of the storm and associated energy input.

3.1   Global positioning system (GPS) and measurements

The U.S government has the baseline configuration for the constellation of around 30 satellites. These satellites are in six Earth-centered orbital planes. The circumnavigation period of a GPS satellite is 11 hours, 58 minutes (a half of a sidereal day). These satellites are equally spaced in each orbital plane and orbital planes are equally spaced around the equatorial plane at a 60° separation with an inclination of 55° relative to the equatorial plane. Their orbital radius is $\sim$ 26 600 km from the center of the Earth. At one point and at a given time
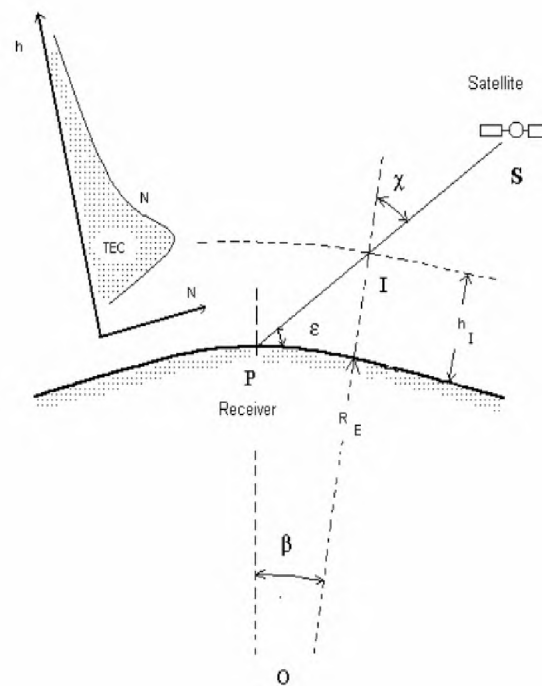
Figure 3.1: Derivation of TEC (Kantor *et al.*, 2006).

on the Earth's surface, at least 4 GPS satellites are visible (Kaplan and Hegarty, 2005). GPS has many applications, such as satellite navigation in vehicles, aircraft and ships. They are used in scientific experiments, and for monitoring geological activities, for example, earthquakes and volcanic eruption (Mio, 2016). GPS is also used to measure TEC, ionospheric scintillation and other parameters which are used in the study of the ionosphere (Yizengaw, 2004). GPS signals may suffer fluctuations due to ionospheric irregularities and reach the receiver through multiple paths.

TEC can be calculated if the electron number density N_e is known. Slant TEC along a ray path from a GPS satellite to a receiver is given by:

$$STEC = \int_P^S N_e(r, \theta, \varphi, t)dr, \tag{3.1}$$

where P is the receiver position, S is the satellite position, r is the radial distance from the center of the Earth to the satellite, θ is the latitude, φ is the longitude and t is the time. Figure 3.1 shows the receiver and satellite's positions, the elevation angle ε and the zenith angle χ of the satellite. The $STEC$ can be converted into $VTEC$ using the following equation:

$$VTEC = \left(STEC - R_B - T_B\right)\left(\sqrt{1 - \left(\frac{R_E cos\varepsilon}{h + R_E}\right)^2}\right) \tag{3.2}$$

where R_E is the radius of the Earth, ε is the elevation angle of the satellite, R_B the correction for receiver biases, T_B is the correction for transmitter biases and $h = 400$ km (the height where the ionosphere is assumed to be a thin shell) (Yizengaw, 2004). By comparing smoothed running mean and calculated values of TEC, the small fluctuations in TEC, which are irregular variations for a specific scale, show irregularities.

3.1.1   Derivation of the GPS TEC

Each GPS satellite transmits 2 carrier signals in the L-band. One signal is transmitted at 154×10.23 MHz (which is L1 = 1575.42 MHz) and with a wavelength of 19 cm. Another is transmitted at 120×10.23 MHz (which is L2 = 1227.60 MHz) and with a wavelength of 24 cm. The travel time of the code and the carrier phase between the satellite and the receiver are used to calculate TEC in the following manner: Let the pseudo-range derived from the code travel time be L (in distance units) and the carrier phase observation be Φ (in distance units).

$$L_i = \delta + c.(dT - dt) + \tau_i^{io} + \tau^{tro} + b_i^{L,r} + b_i^{L,s} + m_i^L + \epsilon_i^L \tag{3.3}$$

and

$$\Phi_i = \delta + c.(dT - dt) + \lambda_i N_i - \tau_i^{io} + \tau^{tro} + b_i^{\phi,r} + b_i^{\phi,s} + m_i^\phi + \epsilon_i^\phi \tag{3.4}$$

with $i = 1$ or 2 for L1 or L2 respectively, δ is the geometrical range between the satellite and the receiver, c is the speed of light in a vacuum, dT and dt are the receiver and the satellite

clock offsets from GPS, $\tau_i^{io} = \frac{40.3TEC}{f_i^2}$, f_i is the carrier frequency, τ^{tro} is the tropospheric delay, $b_i^{L,r}$ are the receiver instrumental delays on L, $b_i^{\phi,r}$ are the receiver instrumental delays on Φ, $b_i^{L,s}$ are the satellite instrumental delays on L, $b_i^{\phi,s}$ are the satellite instrumental delays on Φ, m_i^L are the multipath on L measurements, m_i^ϕ are the multipath on Φ measurements, ϕ_i are the carrier phase observations (in cycles), λ_i are the wavelengths, N_i are the unknown Li integer carrier phase ambiguities, ϵ_i^L are the receiver noises on L and ϵ_i^ϕ are the receiver noises on Φ.

TEC may be calculated in two ways: (a) by subtracting the pseudo-ranges observations L_i:

$$TEC_L = 9.52(L_2 - L_1) + instrumental\ delays + multipath + noise \qquad (3.5)$$

and (b) by subtracting the carrier phase observations Φ_i

$$TEC_\phi = 9.52[(\Phi_1 - \Phi_2) - (\lambda_1 N_1 - \lambda_2 N_2)] + instrumental\ delays + multipath + noise \quad (3.6)$$

where TEC_ϕ is less noisy than TEC_L but has ambiguity of ($\lambda_1 N_1 - \lambda_2 N_2)/2\pi$. The noise of TEC_L increases as the elevation angle (ε) is less than 20°. Equation (3.6) indicates that the phase observations can have sudden changes known as cycle slips, but this can be fixed by cycle slip correction (by adjusting the continuity of $(\Phi_1 - \Phi_2)$). The ambiguity also can be removed by averaging $(TEC_L - TEC_\Phi)$ over a satellite pass. The unambiguous TEC (TEC_u, which only has instrumental delays, multipath and noise) is then given by:

$$TEC_u = TEC_\phi - \langle TEC_\phi - TEC_L \rangle \qquad (3.7)$$

GPS TEC data downloaded from IGS GPS receivers in Antarctica were used for this study. The following links were used for GPS TEC measurements:

1. ftp://geoid.hartrao.ac.za/../rinex/

2. ftp://lox.ucsd.edu/pub/rinex/.

TEC data was derived from GPS measurements using an algorithm developed at Boston College which uses phase and code values for f1 = 1575.42 MHz and f2 = 1227.60 MHz to remove differential clock error effects (Habarulema *et al.*, 2015).

The data of elevation angle $\geq 35°$ (elevation threshold) were used to avoid multipath effects for the TEC data. VTEC values (data) of different PRNs derived at the same time were averaged to one value (data).

3.1.2   Derivation of the GPS scintillation

It is also possible to determine amplitude and phase scintillation indices from GPS measurements by comparing the measured and calculated Doppler shift of frequencies. Irregularities in the ionosphere, large-scale or small-scale can be estimated and recorded (Titheridge, 1963). The amplitude scintillation index S_4 is the square-root of the normalised variance of the received signal power intensity (I) for a given time interval and it is dimensionless. It is given by the following formula (De Jesus et $al.$, 2016):

$$S_4 = \sqrt{\frac{< I^2 > - < I >^2}{< I >^2}} \tag{3.8}$$

The phase scintillation index (σ_ϕ) is the standard deviation of a linearly detrended phase data segment. σ_ϕ is calculated at the time resolution of 1, 3, 10, 30 and 60 seconds. It is given by the following formula:

$$\sigma_\phi = \sqrt{< \phi^2 > - < \phi >^2} \tag{3.9}$$

It is measured either in radians or in degrees and ϕ is the signal phase measured also in radians or in degrees.

$$\phi = \frac{q^2}{2c\epsilon_o m_e f (2\pi)^2} \int n_e d\rho \tag{3.10}$$

$\int n_e d\rho$ is TEC, q is the charge of an electron, m_e is the mass of an electron, ϵ_o is the permittivity of free space, c is the speed of light, and f is the frequency in Hertz (Kintner et $al.$, 2007). In MKS units this reduces to

$$\phi = \frac{40.3}{cf} TEC. \tag{3.11}$$

Ionospheric scintillation is derived using the GPS ionospheric scintillation and the TEC monitor (GISTM) system model GSV4004B. This model has an antenna with an L_1/L_2 GPS

antenna, a GPS receiver and a power supply. The receiver collects 50 raw data per second. The phase is computed in 60 seconds of time resolution. The raw amplitude measurements are also detrended using a 6th order Butterworth high-pass filter or by measurements in averaging 1-minute intervals (for a cutoff frequency of zero). Since total S_4 contains effects of ambient noise as well as multipath effects, the correction of the total amplitude is also computed in 1-minute intervals using the following equation:

$$S_4 = \sqrt{S_{Tot}^2 - S_{cor}^2} \tag{3.12}$$

where S_{Tot} is the total amplitude scintillation and S_{cor} is the corrected amplitude scintillation. The theoretical upper limit of S_4 is 1.0 in a 1-minute interval. The amplitude/phase scintillation is classified in three categories: weak scintillation for S_4 (or σ_ϕ) < 0.3; moderate scintillation for $0.3 \leq S_4$ (or σ_ϕ) > 0.6; and S_4 (or σ_ϕ)$\geq$ 0.6 represents strong scintillation and implies a strong scattering of the signal in the ionosphere (John, 2007; Wang et $al.$, 2016). Weak scintillation has no impact on GPS signals (C.H, 1989). The GPS phase and amplitude scintillation data at SANAE were provided by the South African National Space Agency (SANSA) in Hermanus. Scintillation data were selected by using only data with an elevation angle of $\geq$ 35° in order to avoid non-ionospheric multipath caused by surrounding obstacles.

3.2   SuperDARN HF radars

SuperDARN measures the Doppler velocity, the power, the spectral width and the elevation angle of the targeted object (Oinats et $al.$, 2015). Each SuperDARN radar measures power, Doppler velocity, spectral width and elevation angle (Figure 3.2). By combining the ionospheric Doppler velocity data from the SuperDARN radars and fitting corresponding electric fields into spherical harmonic representation, a convection map can be produced over each hemisphere every 2 minutes (Chisham et $al.$, 2007; Shepherd, 2010; Matsuo and Richmond, 2013). The radars' operating frequencies are selected between 8 and 20 MHz and there are currently 35 radars with most located at the northern and southern pole areas, and a few in the mid-latitudes (Steme et $al.$, 2011; Lester, 2013). Figure 3.3 shows the SuperDARN radars in the southern hemisphere. Most radars have 16 beams, enumerated from 0 to 15
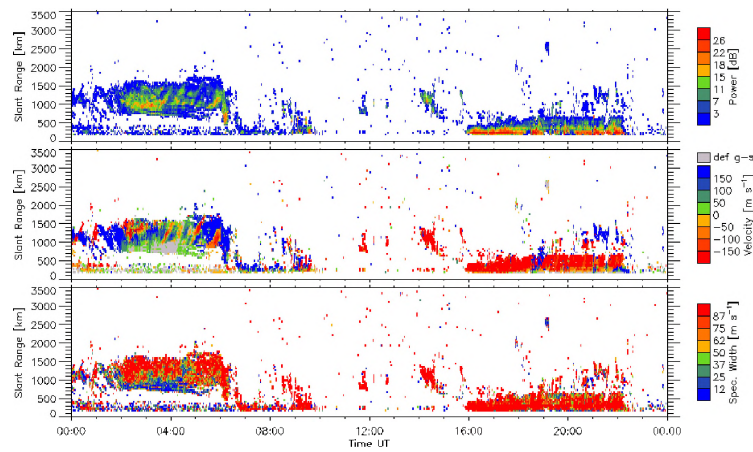
Figure 3.2: Plots of the power (top panel), the velocity (middle panel) and the spectral width (bottom panel) of beam 12 of SANAE SuperDARN on 2013/03/17 (VirginiaTech, 2016).

from left to right respectively but others radars have more. Each beam has its looking direction (Karpachev *et al.*, 2010; Lester, 2013). Each SuperDARN radar transmits ~ 10 kW of peak power, uses multi-pulse sequences to simultaneously determine the range and Doppler velocity and produce identical data products that are routinely combined to produce hemispheric characterisations of ionospheric plasma convection. Power, Doppler velocity and spectral width ground backscatter are used to detect the presence of TIDs whereas convection maps (which use ionospheric scatter) are used to highlight potential source regions of Joule heating. Different shapes (see Figure 3.3) shown in tomato, spring-green and deep-
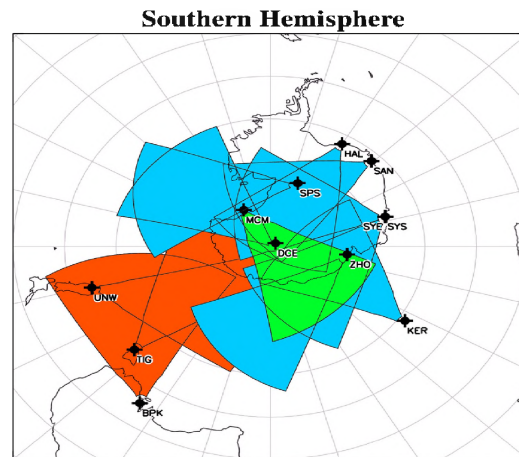
Figure 3.3: The fields-of-view of SuperDARN in the southern hemisphere (VirginiaTech, 2016).

sky-green colours are the FOV of radars for mid-latitude, high latitude and the polar cap respectively. The purpose of mid-latitude radars (see Figure 3.3) is to receive scatters when

the auroral oval containing irregularities shifts from high- to low-latitude, during geomag-
netic storms. SuperDARN HF radars send and receive signals from ionospheric scatter or
from ground backscatter (see Figure 3.4). For a significant amount of time polar radars don't
receive these scatter signals. Backscatter signals may be lost both during absorption or in
the absence of irregularities in the ionosphere (section 3.2), as well as when the auroral oval
expands across the FOV's. In a standard mode, each beams dwelling time is either 3, or 4 or
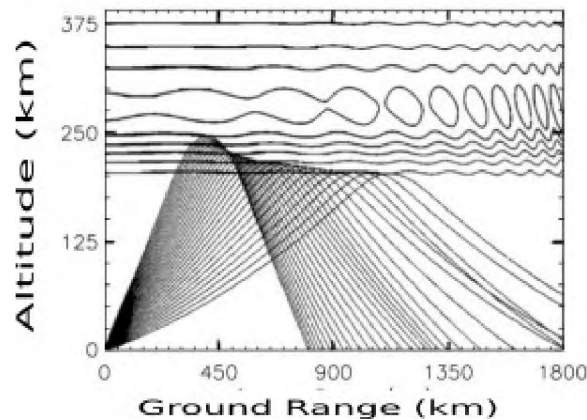
Figure 3.4: The reflection of a radar signal (Grocott *et al.*, 2013).

7 seconds, producing a scan of all 16 beams in 1 or 2 minutes. A phasing matrix is used to
sweep the beam through successive positions with an azimuthal separation of roughly 3.23°,
depending on the operating frequency. For each beam the backscatter power, the line-of-
sight Doppler velocity, and the spectral width is gated up to 75 to 110 cells, which are 45 km
long for standard operation, although there is an initial distance of 180 km for backscatter
from the radar. The spatial coverage of each radar is around 2000×2000 km^2. Each beam
direction receives a 3 dB beam width of $\sim 5°$ and each scan lasts 1 or 2 minutes. Seven or
eight pulses are sent in a pulse train separated by a different multiple of a time lag τ (where
τ is either 2.4 or 1.5 ms). The seven-pulse train yields 27 lags (with 5 missing) which form
the Autocorrelation Function (ACF), for calculating the Doppler velocity and the spectral
width. Figure 3.2 shows examples of these measurements as a function of universal time
(UT) and the slant range (in km) above the radar. The transmitters of SuperDARN send
out a series of pulses and these pulses are sampled by the receivers. The complex ACF is used
to analyse these pulses. Examples of two pulse sequences will be used to demonstrate how
the characteristics of the scattering plasma waves (power, velocity and spectral width) can
be estimated at a certain distance d_0 in the ionosphere. The irregularities in the plasma act
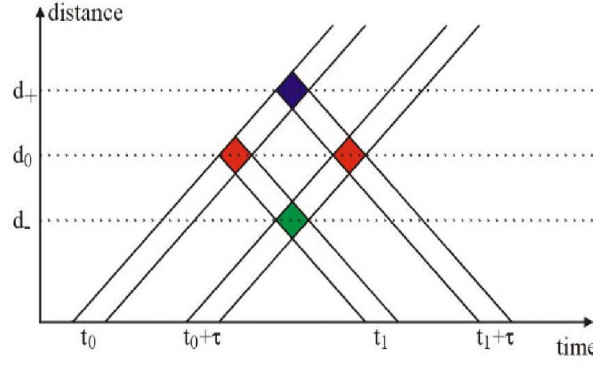
Figure 3.5: The SuperDARN pulses (Kathryn McWilliams, 2003).

as the reflectors of the signals. Let τ be the time between the transmission of two separate pulses. During this time the plasma is also in motion. This means that P_1 is sent at time t_0 and P_2 is sent at $t_0 + \tau$. The pulse P_1 is received from d_0 at time t_1, P_1 is received from d_+ at time $t_1 + \tau$, P_2 is received from d_- at time t_1 and P_2 is received from d_0 at time $t_1 + \tau$ (see Figure 3.5). The amplitude $A(t_1)$ measured at t_1 is given by the following equation:

$$A(t_1) = A_1(d_0) + A_2(d_-) \tag{3.13}$$

The amplitude $A(t_1 + \tau)$ measured at $t_1 + \tau$ is given by the following equation:

$$A(t_1 + \tau) = A_1(d_+) + A_2(d_0) \tag{3.14}$$

The ACF at lag τ is given by the following equation:

$$A(t_1).A(t_1 + \tau) = \big(A_1(d_0) + A_2(d_-)\big).\big(A_1(d_+) + A_2(d_0)\big) \tag{3.15}$$

To minimise uncorrelated signal (phases), the average ($\langle \rangle$) of many return signals is:

$$\langle A(t_1).A(t_1 + \tau) \rangle = \langle A_1(d_0).A_1(d_+) \rangle + \langle A_1(d_0).A_2(d_0) \rangle + \langle A_2(d_-).A_1(d_+) \rangle + \langle A_2(d_-).A_2(d_0) \rangle \tag{3.16}$$

A good estimation of the average is made, if the ionosphere is correlated at distance d_0 over the averaging time.

$$\langle A(t_1).A(t_1 + \tau) \rangle \sim \langle A_1(d_0).A_2(d_0) \rangle \sim A \exp(i\omega\tau) \tag{3.17}$$

For each lag (in phase and quadrature voltages), the real and imaginary contribution is measured. By using the Fourier transform of the ACF, the spectrum is produced. The Doppler velocity and backscattered power are estimated by using the FITACF routine. Assuming that the ACF amplitude decays exponentially:

$$A(\tau) = A_0 \exp\left(-\frac{\tau}{t_d} + i2\pi\tau f_d\right) \tag{3.18}$$

where t_d is a decay time constant, $f_d = \frac{1}{2\pi}\frac{\partial\phi}{\partial\tau}$ and $i = \sqrt{-1}$. Its absolute value is given by:

$$|A(\tau)| = A_0 \exp\left(-\frac{\tau}{t_d}\right) \tag{3.19}$$

The phase ϕ at lag τ is given by (Kathryn McWilliams, 2003; Ribeiro et $al.$, 2013):

$$\phi(\tau) = arctan\left(\frac{Im(A(\tau))}{Re(A(\tau))}\right) \tag{3.20}$$

3.2.1   SuperDARN power

The SuperDARN power is the logarithm of the ratio of signal power to noise power (signal-to-noise ratio (SNR) in dB), as shown in the top panel of Figure 3.2 (Hayashi et $al.$, 2010). The lag power at lag τ is given by:

$$P(\tau) = |A(\tau)| \tag{3.21}$$

$$SNR = 10\log_{10}\left(\frac{A_0}{N}\right) \tag{3.22}$$

where A_0 is the fitted lag zero power and N is the noise power level.

3.2.2   Doppler velocity

From the equation 3.20, the Doppler velocity v, as shown in the middle panel of Figure 3.2, is calculated by using the following equation:

$$v = \frac{\lambda}{4\pi}\frac{\partial\phi}{\partial\tau} \tag{3.23}$$

where λ is the radar wavelength. In order to measure the relative velocity between the targeted object and the radar, the Doppler effect is used. The radar sends a signal wave to the object and the object reflects the signal to the source. If the wave has to move farther, the gap between each wave increases, increasing the wavelength. The wavelength decreases as the object approaches a fixed (not moving) radar. The change in frequency observed by a radar due to a target moving at relative velocity can be calculated, provided the waves' frequency sent by a radar is f_o, and the observer detects the waves at frequency f. The velocity of a targeted object is given by v and the velocity of the source (radar) is given as v_s. In general, the Doppler relation is given by (Iyer and Prabhu, 2013):

$$f = \left(\frac{c + v}{c + v_s}\right) f_o \tag{3.24}$$

where c is the speed of light in a vacuum. The Doppler velocity corresponds to the line-of-sight plasma velocity in the case of ionospheric scatter or to the vertical motion of the ionosphere in the case of ground scatter. Assuming that the reflection points of radar waves move with the winds associated with neutral particles (Susumu, 2005), the Doppler velocity at a given location in the atmosphere is defined to be equal to the radial component of the wind at that location:

$$\mathbf{V_r} = V.\mathbf{r} \tag{3.25}$$

where $\mathbf{r}$ is the unit vector (pointing direction of the radar) and V is the wind speed. The positive value of the ground/sea scatter echo Doppler velocity observed with a SuperDARN radar corresponds to the downward ionospheric motion. The negative value of the ground/sea scatters echo Doppler velocity observed with a SuperDARN radar corresponds to the upward ionospheric motion (see the middle panel of Figure 3.2). The real vertical speed (v_{vert}) of the ionosphere is given by:

$$v_{vert} = \frac{v}{2sin\varepsilon} \tag{3.26}$$

where ε is the elevation angle (Hayashi et $al.$, 2010; Oinats et $al.$, 2015).

3.2.3 Convection maps

The transmitted high-frequency (HF) radar waves are refracted in the ionosphere and can therefore achieve perpendicularity to the Earth's magnetic field over large areas into the polar latitudes. The ionospheric convection patterns in high latitudes are derived by using line-of-sight plasma drifts data from the SuperDARN. The solar wind, IMF and dipole tilt angle conditions are used to get discrete patterns which are interpolated and give a dynamical model of convection, specifying the high-latitude electrostatic potential distribution for a wide range (Shepherd, 2010). Therefore, SuperDARN HF radars are able to measure Doppler velocity of meter-scale F_2-region irregularity backscatter moving with the ambient plasma at $\mathbf{E} \times \mathbf{B}$ convection velocity ($\mathbf{v}$) using:

$$\mathbf{v} = \frac{\mathbf{E} \times \mathbf{B}}{B^2} \tag{3.27}$$

where

$$\mathbf{E} = -\nabla\Phi \tag{3.28}$$

$\mathbf{E}$ is the electric field, Φ is the electrostatic potential, $\mathbf{B}$ is the magnetic field and B is the magnitude of the magnetic field (Yeoman *et al.*, 2008).

The enhancement of Joule heating during periods of strong IMF may cause polar cap gravity waves and auroral infrasonic waves associated with intense particle precipitation in the electrojets as suggested by McHarg et al. (2005). These gravity waves are identified by rocket flights, lidars, GPS, or VHF and UHF radars. The gravity wave observations are visualised in terms of vertical wavelength or frequency spectra of atmospheric velocity fluctuations. These thermospheric gravity waves may affect radio waves propagation. These gravity waves contribute to individual peaks of power spectra, after considering ground-backscattered power and velocity (Vadas *et al.*, 2012; Valladares and Hei, 2012). The spectra are obtained from the SuperDARN data by analysing perturbations of the ground-backscattered power and velocity. The plasma flow along magnetic field line reflects in the line-of-sight Doppler velocity by which radars are able to measure (Bristow and Greenwald, 1997). At high latitude, thermospheric gravity waves in their horizontal motion, are one of the sources of LSTIDs during geomagnetic storms. These TIDs signatures are observed in TEC fluctuations and as a sequence of enhancement and depletion in the SuperDARN measurements (the power,

velocity and spectral width).

Figure 3.6 shows examples of convection maps (obtained from http://vt.superdarn.org/tiki-index.php), which show the following information: color-coded velocity vectors indicate fitted velocities at the locations of the lines-of-sight Doppler velocity data; the contours of constant electrostatic potential (solid blue and dashed red lines) represent the flow streamlines for the whole polar ionosphere. The convection pattern consists of 2 convection cells with antisunward flow across the polar cap that returns to the dayside via sunward flow on the dawn and dusk flanks. The maps are presented in a magnetic local time (MLT) coordinate system, such that the magnetic local midnight is at the bottom, noon at the top, dawn to the right and dusk to the left. The small dots at one end of the velocity vectors show the vector locations and the lines indicate the vector magnitudes and directions. The projection of the IMF (red arrow) and its magnitude into Y-Z plane are found at the top right of the maps. The negative sign (-) and positive sign (+) show the regions of minimum and maximum electrostatic potentials respectively. The maximum potential difference across the polar cap (Φ_{PC}) is shown at the bottom right of each figure. The velocity color scale (violet to red) is indicated at the top left of convection maps and the number of radars is shown at the bottom left. At the top middle of each convection map, there is day, month, year and the universal time by which the flows were modelled or measured (Yeoman *et al.*, 2008; Shepherd, 2010; Matsuo and Richmond, 2013).

LSTIDs can also be defined, for electron density in the ionosphere, as transient perturbations given by the AGWs giving ground backscattered power with the conjunction of the SuperDARN signals (Karpachev *et al.*, 2010). During geomagnetic storms, a LSTID passing through the radar's field of view (FOV) leads to a HF wave focusing or defocussing effects (Chisham *et al.*, 2007; Hayashi *et al.*, 2010; Oinats *et al.*, 2015). The effects of focusing or defocussing of signal waves might cause the lack of backscatter in the SuperDARN radars during these strong geomagnetic storm. During a major geomagnetic storm at the high-latitude, auroral oval shifts equatorward of FOVs of radars and causes the lack of backscatter. The reason behind the lack of backscatter is that most of the irregularities responsible for reflection of radar's radiations are in the auroral oval.
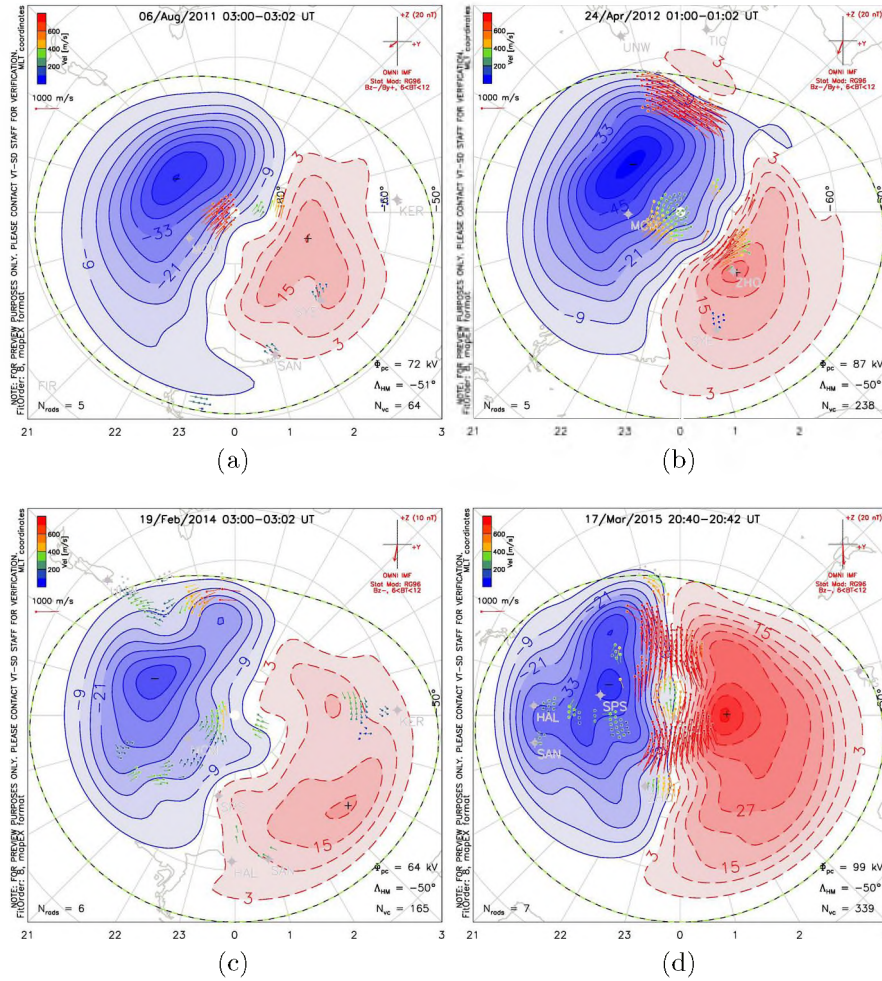
Figure 3.6: The sample of convection maps (a) on 2011/08/06 at 03:00, (b) on 2012/04/24 at 01:00 (c) on 2014/02/19 at 03:00 and (d) on 2015/03/17 at 20:40

In order to determine LSTID from the SuperDARN power, the spectra content of the time series of the data was determined by a fast Fourier transform (FFT) with an interactive data language (IDL) routine. The gaps of data were populated by interpolating with a running box car averaged over 180 minutes. The frequency f, with 0.1 mHz $< f < 0.9$ mHz band pass filter to the spectrum and the data sampling rate of 60 seconds was used. The IDL native routine DIGITAL FILTER was used to isolate the frequency range of interest. Finally, -50 dB was selected for the Gibbs phenomena peaks resulting from the filter. Gibbs phenomenon is defined as "the peculiar manner in which the Fourier series of a piecewise continuously differentiable periodic function behaves at a jump discontinuity" (Jerri, 2013).

3.3   Magnetic indices

In this study the minimum Dst $\leq$ -100 nT was used to characterise strong and severe geomagnetic storms. The data output of Dst and AE indices (Hourly Values) may be found online at (http://wdc.kugi.kyoto-u.ac.jp/dstae/index.html). The AE index is the value of geomagnetic variation in the horizontal component in the auroral region.

$$AE = AU - AL \tag{3.29}$$

where AU and AL are the upper and the lower limits of the envelopes of the averaged values of horizontal components from different stations. The AU and AL indicate the strongest current intensity of the eastward and westward auroral electrojets, respectively (Hargreaves, 1992; Kyoto, 2015).

3.4   Summary

This chapter described the methods used by GPS and SuperDARN HF radars to derive the used data. It described also the data processing until used to give the results containing in the next chapter. The GPS data, the SuperDARN data, the Dst index and the AE index were explained in detail in this chapter. Data from four GPS stations in Antarctica were used to analyse 14 storm cases for their ionospheric responses. These will be discussed in the next chapter.

Chapter 4

Results and discussion

In this chapter, the findings on the different ionospheric storm responses at SANAE and its surrounding stations during intense storms (i.e. Dst $\leq$ -100 nT) during 2011-2015 are presented. The study aims to contribute to the understanding of the nature of ionospheric disturbances associated with geomagnetic storms, using GPS TEC and scintillation measurements, SuperDARN HF radar measurements and their ionospheric convection maps. The ionospheric responses to geomagnetic storms that will be discussed are storm effects, phase and amplitude scintillation and TIDs. Figure 4.1 shows the geographic coordinates of the GPS receivers (with dark-green dots and yellow diamond for SANAE station) and the SuperDARN HF radars (with blue diamond and yellow diamond for SANAE radar). Table 4.1 lists the geographic and geomagnetic coordinates of GPS receivers and SuperDARN HF radars.

Table 4.2 presents the magnitude and duration of all storms studied. Note that in this study the end of the recovery phase of a storm is defined as when Dst $>$ -50 nT. This table shows that 78.6% of these storms took place between 00:00 UT and 09:00 UT, local morning, and 21.4% of such storms took place between 19:00 UT and 23:00 UT, local night at SANAE (note that SANAE local time (LT) is equivalent to UT). The majority of the storms (57.1%) lasted for a period of between 22 and 48 hours, about 28.6% of the storms lasted for a period of between 2 and 3 days and 14.3% of the storms lasted for a period of between 4 and 6 days. 7.1% of the storms had a duration of less than a day, but the majority (92.9%) lasted longer. Table 4.2 also shows that 28.6%, 35.7%, 28.6% and 7.1% of the storms occurred in winter, spring, autumn and summer respectively.
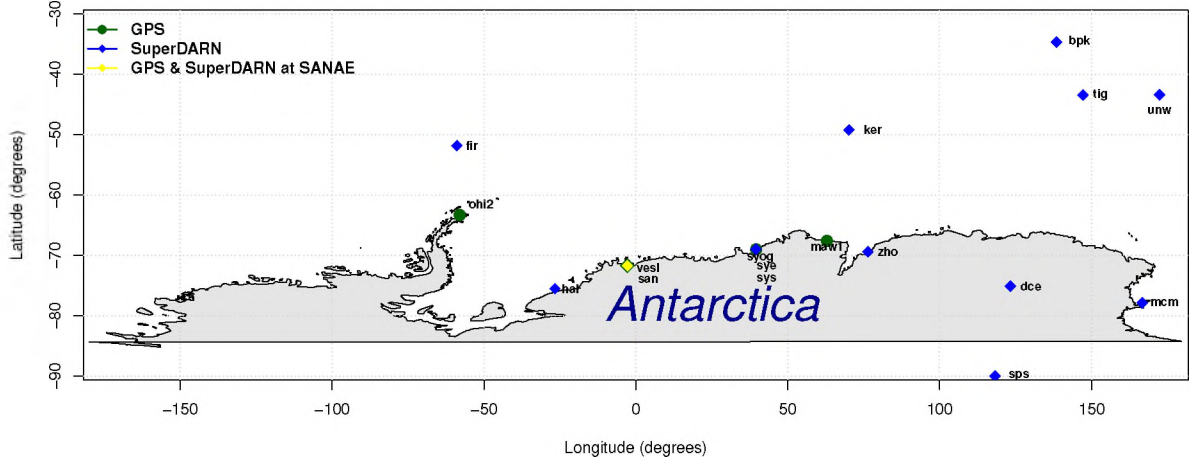
Figure 4.1: IGS GPS receivers on Antarctica and the SuperDARN HF radars in the southern hemisphere

The storm effects are presented in terms of percentage deviation of $Vtec$ ($dVtec$) from the 28-day running median of $Vtec$ ($Vtec_{median}$) centered on the day of the storm, as expressed by equation (4.1) (Yizengaw, 2004; Buresova and Lastovicka, 2008):

$$dVtec = \frac{Vtec - Vtec_{median}}{Vtec_{median}} \times 100 \qquad (4.1)$$

Negative storm effects are defined by $dVtec \leq$ -45% and positive storm effects are defined by $dVtec \geq$ 45%, as in the studies by Buresova and Lastovicka (2008) and by Matamba et al. (2015). Note that $Vtec$ at each epoch is calculated as an average of vertical TEC from all PRNs within the FOV of the GPS receiver at that epoch. These studies found that the thresholds are sufficiently large to prevent inclusion of the random perturbations and disturbances of the neutral atmospheric origin (gravity waves, etc).

4.1   Ionospheric storm effects

The effects of major storms are grouped into three categories: the negative, the positive and the combination of negative and positive storm effects (Tsagouri et al., 2000; Burns et al., 2007). Effects of less than 20 minutes duration were considered insignificant and were thus

Table 4.1: Geographic and geomagnetic coordinates of GPS and SuperDARN stations used in this study

GPS and Super-DARN HF radar stations	Geographic Latitude (°)	Geographic Longitude (°)	Geomagnetic Latitude (°)	Geomagnetic Longitude (°)	Code
GPS and their locations					
SANAE	-71.67	-2.84	-61.17	43.23	vesl
Syowa	-69.01	39.38	-66.04	71.51	syog
Mawson	-67.60	62.87	-70.12	89.78	maw1
O'Higgins2	-63.32	-57.90	-48.29	12.22	ohi2
SuperDARN HF radars and their locations					
Buckland Park	-34.62	138.46	-46.09	-146.41	bpk
Dome C	-75.09	123.35	-88.69	54.43	dce
Falkland Islands	-51.83	-58.98	-37.62	9.89	fir
Halley	-75.52	-26.63	-61.33	29.04	hal
Kerguelen	-49.22	70.14	-58.34	121.82	ker
McMurdo	-77.88	166.73	-79.92	-32.71	mcm
SANAE	-71.68	-2.85	-61.17	43.22	san
South Pole Station	-89.995	118.291	-73.97	18.84	sps
Syowa East	-69.0	39.58	-66.5	72.2	sye
Syowa South	-69.0	39.58	-66.5	72.2	sys
Tiger	-43.40	147.2	-54.72	-133.46	tig
Unwin	-46.51	168.38	-54.4	-106.41	unw
Zhongshan	-69.38	76.38	-74.51	96.03	zho

neglected.

An example of the implementation of this analysis is given in Figure 4.2 and it applies
to all 14 of the storms studied. This figure shows the comparison of *Vtec* (in dark-green
lines) with the $Vtec_{median}$ (in blue) for the period 28/09 - 04/10/2012 of a storm with the
minimum Dst of -119 nT. The 3 vertical lines in these figures show the commencement of
the initial phase (IP), the commencement of recovery phase (RP) and the end of RP. Fig-
ure 4.2(b) shows, during the main phase (MP) of this storm, a combination of positive and
negative storm effects at the Mawson and SANAE stations, whereas O'Higgins2 and Syowa
stations only show positive storm effects. Negative storm effects manifested at Mawson,
Syowa and SANAE stations during the recovery phase. This example also illustrates that a

Table 4.2: Geomagnetic storms (Kyoto, 2015).

Major geomagnetic storms between 2011 and 2015				
Storm day	Minimum Dst index (nT)	UT of min- imum Dst index	Duration of storm (Date and UT)	Season
2011/08/06	-115	04:00	2011/08/05 (17:00)-2011/08/07 (16:00)	winter
2011/09/27	-118	00:00	2011/09/26 (11:00)-2011/09/27 (14:00)	spring
2011/10/25	-147	02:00	2011/10/24 (17:00)-2011/10/26 (08:00)	spring
2012/03/09	-131	09:00	2012/03/08 (11:00)-2012/03/10 (16:00)	autumn
2012/04/24	-108	05:00	2012/04/23 (00:00)-2012/04/25 (00:00)	autumn
2012/07/15	-127	19:00	2012/07/14 (16:00)-2012/07/17 (10:00)	winter
2012/10/01	-119	05:00	2012/09/30 (10:00)-2012/10/01 (18:00)	spring
2012/10/09	-105	09:00	2012/10/07 (02:00)-2012/10/09 (17:00)	spring
2012/11/14	-108	08:00	2012/11/13 (02:00)-2012/11/14 (18:00)	spring
2013/03/17	-132	21:00	2013/03/17 (10:00)-2013/03/18 (09:00)	autumn
2013/06/01	-119	09:00	2013/05/31 (15:00)-2013/06/01 (21:00)	winter
2014/02/19	-112	09:00	2014/02/18 (11:00)-2014/02/19 (16:00)	summer
2015/03/17	-223	23:00	2015/03/17 (03:00)-2015/03/21 (03:00)	autumn
2015/06/23	-195	05:00	2015/06/21 (14:00)-2015/06/26 (22:00)	winter

storm effect may vary with geomagnetic location and time of day at the station. The AE
indices show an enhancement of both eastward and westward auroral electrojets to around
1000 nT, indicating a large energy injection into the polar ionosphere (Figure 4.2(b)).
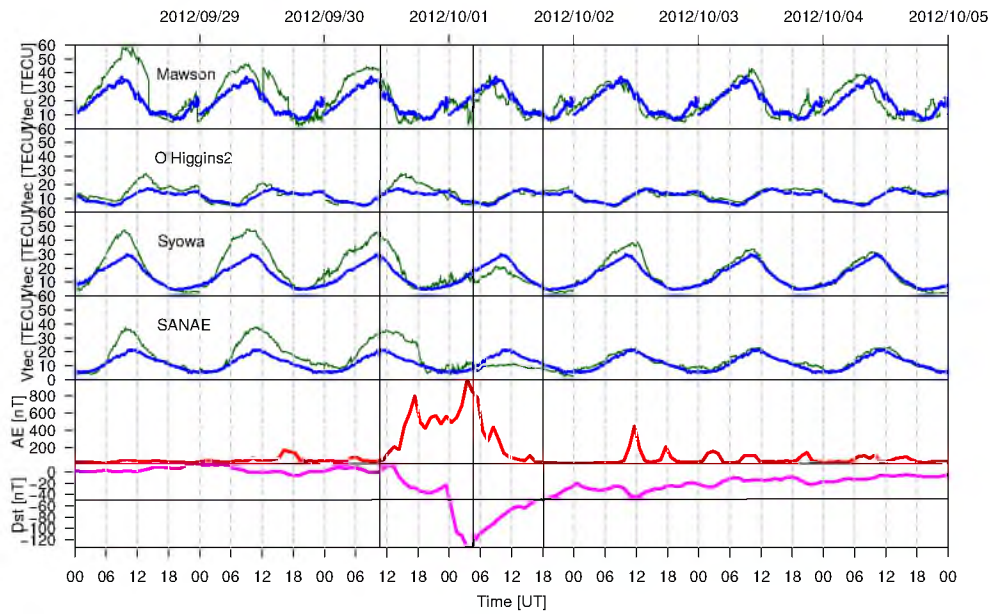
(a)
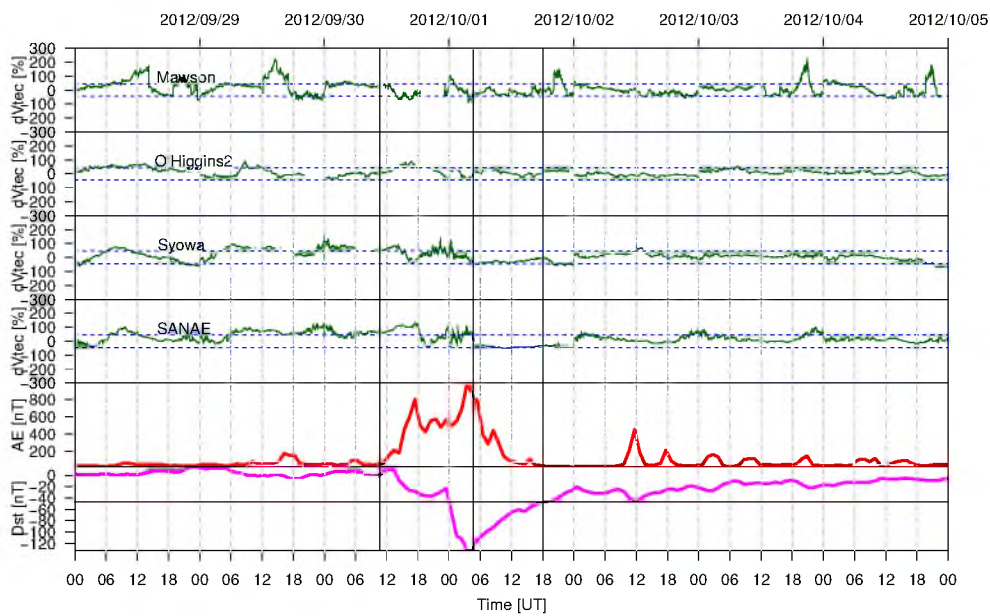
(b)

Figure 4.2: (a) The comparison of Vtec with the 28-day running median of Vtec for 4 stations and (b) the responses calculated for Mawson, O'Higgins, Syowa and SANAE GPS stations for 2012/10/01

4.1.1 Negative ionospheric storm effects and their mechanisms

The ionospheric storm effects are summarised in Table 4.3, based on the season of the storm day and in Table 4.4, based on the phases of the storms. Twenty negative storm effects were

estimated for the 14 storm days over four GPS stations located in Antarctica. The minority (35.0%) of these storm effects lasted between 4 and 12 hours and 65.0% lasted between 20 minutes and 4 hours, as shown in Figure 4.3(a). Considering the individual storm at each station, Table 4.5 shows that 79.0% of the minimum amplitudes had a percentage deviation of -70.0% of their $Vtec$ (dVtec), while 21.0% of the minimum amplitudes had between -34.0% and -70.0%. About 65.0% of the negative storm effects took place in autumn, 5.0% in sum-

Table 4.3: Number of ionospheric storm effects by season at Mawson, O'Higgins, Syowa and SANAE GPS stations

Storm effects and their seasonal occurrence				
Season	Negative storm effects	Positive storm effects	Combination storm effects	Total	%
Summer	1	0	7	8	3.6
Autumn	13	4	65	82	36.4
Winter	0	23	48	71	31.6
Spring	6	3	55	64	28.4
Total	20	30	175	225	100
%	8.9	13.3	77.8	100	—

mer, 30.0% in spring and there was no negative storm effects in winter. During IP and IMP, there were no negative storm effects, but during MP 60%, during MRP 5.0% and during RP 35.0% occurred.

A negative storm effect was observed by Jin *et al.* (2014) from Beidou GEO satellite observations, following the SSC and recovery phase of the 2013/03/17 storm, especially in the southern hemisphere. This observation confirms our observation at Syowa station for the same storm day; however at this station a negative storm effect was also found during the main phase. Similarly, Shreedevi *et al.* (2016) studied the effects of the 2014/02/19 intense storm, by means of GPS-TEC data from the Indian Antarctic station, Bhari (-69.4°, 76.2° geographic coordinates). Dissimilar to our analysis of the same storm, they found a negative ionospheric storm effect starting at around 03:30 Indian Standard Time (IST). They linked the negative storm effect to changes in the global wind system and the storm-induced in the composition changes of gases (Shreedevi *et al.*, 2016).

A study by Prölss *et al.* (1988) suggested that Joule heating due to the collisions of the

particles and neutrals increases the temperature of the ionosphere leading to decreasing electron concentration. The electron concentration is directly proportional to the $\frac{[O]}{[N_2]}$ ratio (i.e. the decrease of this ratio implies the depletion of electron density in a medium). A study by Balan *et al.* (2013) discusses mechanisms of ionospheric storms at the equatorial and high latitudes. Using CHAMP Ne and GPS-TEC data and the Sheffield University Plasmasphere Ionospheric Model, they found that during a geomagnetic storm at high latitudes, the upwelling effect of the wind reduces the $\frac{[O]}{[N_2]}$ ratio (largely increases N_2), with the inward $\mathbf{E} \times \mathbf{B}$ drift resulting in severe negative storm effects in these regions. The global $\frac{[O]}{[N_2]}$ ratio of the 2015/03/17 storm discussed in this study is shown in Figure 4.4, which compares the day before a storm (a), the days during a storm (b) and (c) and the day after the storm (d) respectively. This figure shows that there was a decrease in the $\frac{[O]}{[N_2]}$ ratio during the storm, which extended from the high lats to some parts of the low lats (Asian sector). This decreasing ratio lasted for several days, until 2015/03/23. The increase of the polar cap

(a)

(b)

(c)
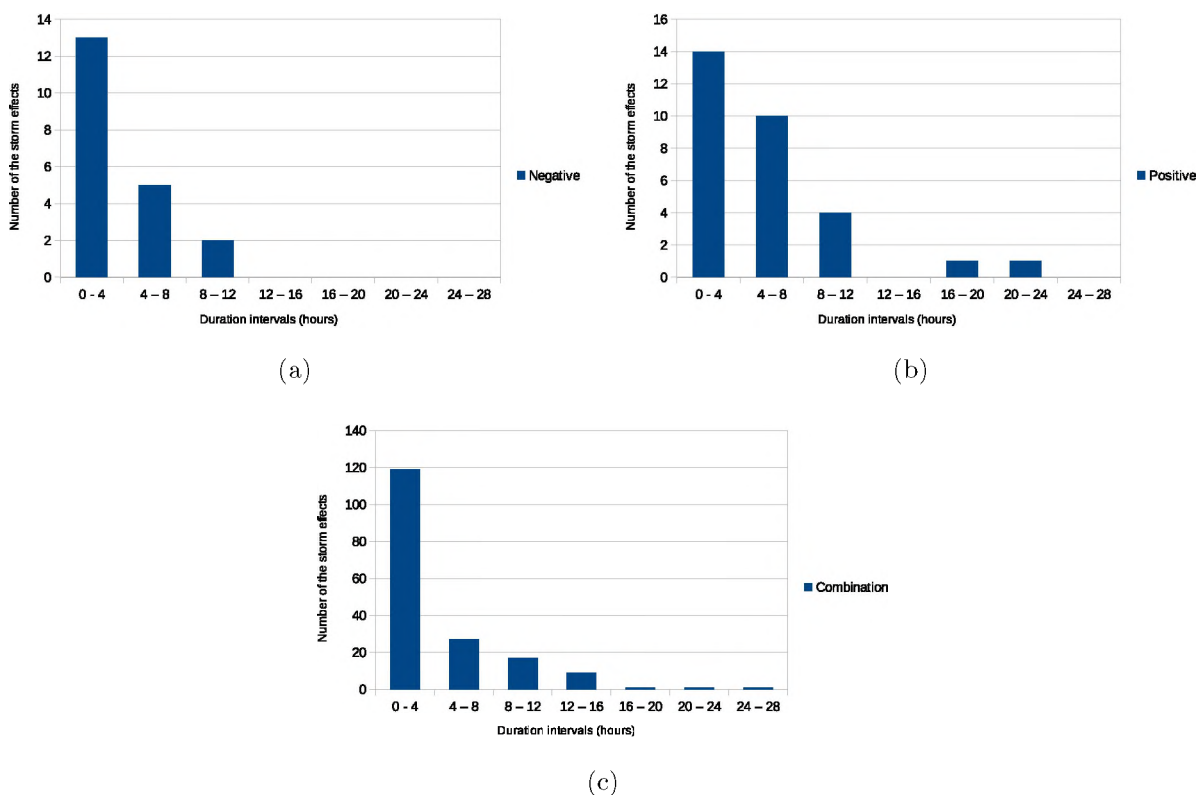
Figure 4.3: (a) The negative, (b) the positive and (c) the combination of negative and positive storm effects and their durations

potential drop caused by the geomagnetic storm, leads to an increase in energy input at the
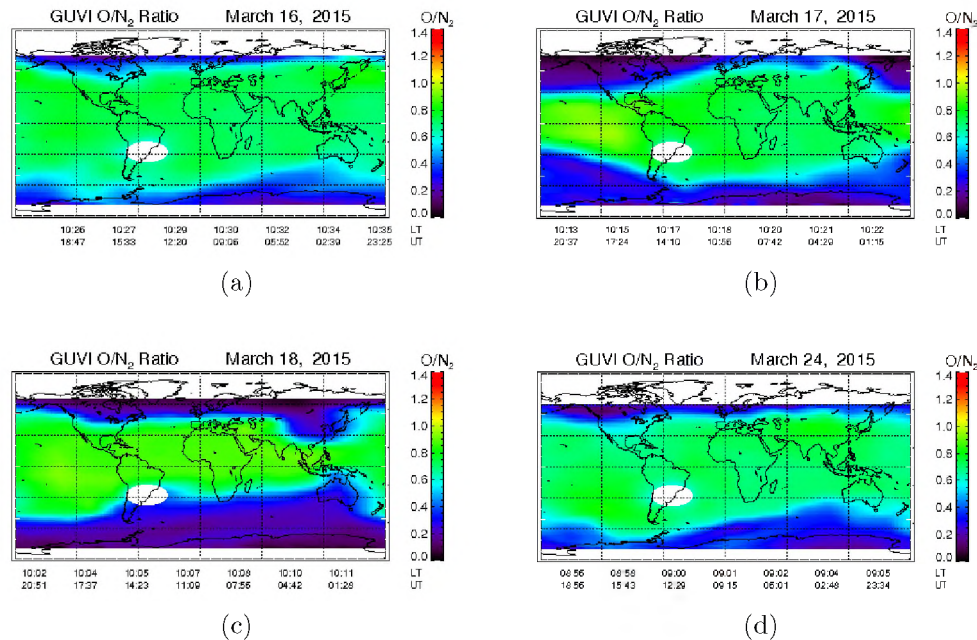
Figure 4.4: The global map of oxygen to nitrogen ratio (a) before, (b) and (c) during and (d) after the 2015/03/17 severe storm (Hopkins, 2016)

Table 4.4: Ionospheric storm effects and the storm phases during which they occurred at Mawson, O'Higgins, Syowa and SANAE GPS stations

The storm effects and the phases during which they occurred					
Phases	Negative storm effects	Positive storm effects	Combination storm effects	Total	%
Initial phase (IP)	0	0	3	3	1.3
Main phase (MP)	12	12	81	105	46.7
Initial & main phase (IMP)	0	0	2	2	0.9
Main and recovery phases (MRP)	1	4	17	22	9.8
Recovery phase (RP)	7	14	72	93	41.3
Total	20	30	175	225	100
%	8.9	13.3	77.8	100	—

high latitudes and causes the expansion of the atmosphere. This expansion of the atmosphere causes the movement of the air by means of constant pressure surfaces and reduces the atom-to-molecule ratio as the air of differing compositions is lifted to higher altitudes. Burns *et al.* (2007) discussed the challenges and successes of the ionospheric response to coronal mass ejections. They found that negative storm effects are caused by temperature and composition changes.

Table 4.5: Minimum and maximum amplitudes of the storm effects over the GPS stations

Storm days and stations in Antarctica								
Storm day	**Maw1**	**Maw1**	**Ohi2**	**Ohi2**	**Syog**	**Syog**	**vesl**	**vesl**
	Min	**Max**	**Min**	**Max**	**Min**	**Max**	**Min**	**Max**
2011/08/06	-	-	-70.6%	62.0%	-41.0%	170.0%	-75.0%	306.0%
2011/09/27	-60.0%	475.0%	-71.0%	321.0%	-84.0%	251.0%	-71.6%	110.5%
2011/10/25	-72.0%	307.0%	-57.0%	205.0%	-75.0%	103.0%	-75.0%	125.0%
2011/03/09	-71.0%	466.0%	-44.0%	117.0%	-78.0%	131.0%	-89.8%	72.0%
2012/04/24	-86.0%	782.0%	-69.0%	179.0%	-78.0%	134.0%	-75.0%	167.0%
2012/07/15	-87.7%	586.0%	-34.0%	268.0%	-70.0%	87.0%	-40.0%	157.5%
2012/10/01	-87.0%	228.0%	-41.0%	90.0%	-71.0%	158.0%	-52.0%	132.0%
2012/10/09	-78.0%	443.0%	-92.0%	217.0%	-64.0%	109.7%	-86.0%	95.0%
2012/11/14	-83.6%	253.0%	-64.8%	94.0%	-79.0%	92.0%	-97.0%	162.0%
2013/03/17	-76.0%	359.0%	-73.0%	157.7%	-80.0%	69.5%	-	-
2013/06/01	-99.6%	199.0%	-80.0%	34.0%	-70.0%	80.0%	-	-
2014/02/19	-93.4.0%	166.0%	-54.0%	111.7%	-99.6%	327.0%	-79.0%	180.7%
2015/03/17	-90.6%	299.0%	-74.7%	273.0%	-100.0%	213.0%	-72.8%	151.0%
2015/06/23	-67.0%	300.8%	-71.0%	183.8%	-81.0%	302.0%	-75.6%	285.0%
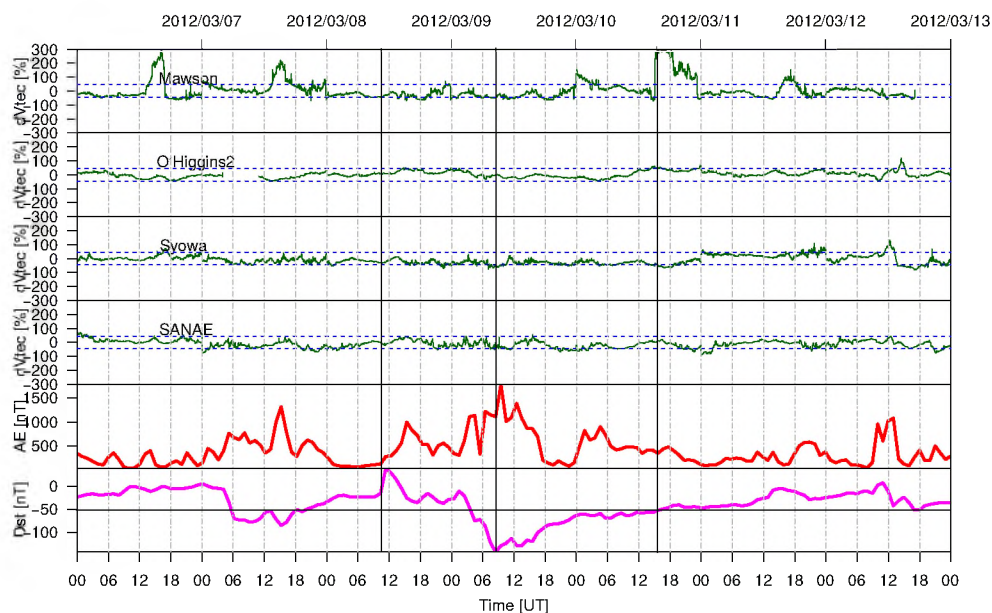
Figure 4.5: The responses calculated from Mawson, O'Higgins, Syowa and SANAE GPS stations on 2012/03/09 storm day.

4.1.2   Positive ionospheric storm effects and their mechanisms

Thirty positive storm effects were calculated over 14 storm days from data for four GPS stations in Antarctica. Figure 4.3(b), Table 4.3 and Table 4.4 summarise their individual durations, their occurrence by season and their occurrence during different phases, respectively.

46.7% of the positive storm effects had a duration between 20 minutes and 4 hours, while 53.3% had a duration between 4 and 24 hours. Looking at the individual storm, 22.6%, 18.9%, 39.6% and 18.9% of the maximum amplitudes had percentage deviations of *Vtec* above 300.0%, between 200.0% and 300.0%, between 100.0% and 200.0% and between 34.0% and 100.0% respectively, as shown by Table 4.5. 13.3% of these storm effects occurred in autumn, 76.7% in winter, 10.0% in spring. There was no positive storm effect in summer for this period. 40.0% of the positive storm effects took place during the MP, 13.3% during the MRP, 46.7% took place during the RP of the storms. There was no positive storm effect during IP and IMP of the storms. When comparing these results to the ones of the negative storm, the positive storm effects have higher amplitudes, these effects are double during the RP and they are more dominant in winter than in other season.

The enhancement of the electric field from the magnetosphere and the horizontal thermospheric circulation which lifted up the plasma contributed to the drift of the F_2-region and enhanced the electrons. The TADs/TIDs caused by energy injection into the upper atmosphere cause the positive storm effects into this region during their equatorward propagation (as shown in section 4.2). The TADs may also cause the vertical drifts which cause the positive storm effects for a short time (Fuller-Rowell *et al.*, 1994; Danilov and Lastovicka, 2001; Huang *et al.*, 2005).

A study by Burns *et al.* (2007) discusses the challenges and successes of the ionospheric response to coronal mass ejections. They found that the positive storm effects could be caused by the neutral wind, the penetration of electric fields and neutral gas compositions. A study by Huang *et al.* (2005) looked at the strong positive phase of ionospheric storms observed by the Millstone Hill incoherent scatter radar and the GPS network. They suggested that electric fields generated the observed positive storm phase.

4.1.3 Combination of the negative and positive ionospheric storm effects and their associated mechanisms

The most frequently observed storm effect was the combination of negative and positive effects (i.e. when a station records both negative and positive effects for a particular storm).

One hundred and seventy-five storm effects over each of four GPS station were calculated during the intense magnetic storms. The majority of these (37.2%) were observed in autumn, 31.4% occurred in spring, 27.4% occurred in winter and the minority (4.0%) occurred in summer, as shown in Table 4.3. About 46.3% of the combination of negative and positive storm effects took place during the MP, 1.8% during the IP, 1.1% during the IMP, 9.7% during the MRP and 41.1% took place during the RP, as shown by Table 4.4. The individual durations of these storm effects are shown by Figure 4.3(c), where 68.0% had a duration of between 20 minutes and 4 hours and 22.0% had a duration of between 4 and 28 hours. In general, the amplitudes of positive effects were higher than the ones of the negative effects.

Many studies found similar results for the combination of negative and positive storm effects of the same geomagnetic storms considered for this study. For example, Klimenko *et al.* (2015) compared GSM TIP model calculations with observations of the ionospheric parameters. Their results confirmed the classical mechanisms associated with positive and negative ionospheric storms for the MP of the 2011/09/27 geomagnetic storm. They suggested that at high latitudes, the electron density is disturbed because of changes in the neutral composition of the thermosphere, leading to the enhancement in the chemical loss rates, and the electromagnetic drift resulting in horizontal plasma transfer.

A comparison of the 2013/03/17 and 2015/03/17 intense storms by Rodriguez-Bouza *et al.* (2016) showed that both storms had a positive ionospheric storm during their main phase, followed by a negative ionospheric storm during the recovery phase. This was also the case in the 2015/03/17 storm at O'Higgins2 station. For other stations a positive ionospheric storm sometimes occurred during both the main and recovery phases. Also these results mutually confirm the fact that the amplitude of the percentage deviation in Vtec is higher for 2015/03/17 than for 2013/03/17, except at Mawson station where the amplitude is higher for 2013/03/17 than for 2015/03/17, for the positive ionospheric storm, as shown in Table 4.5. Adimula *et al.* (2016) using GPS measurements from the IGS database, investigated the ionospheric responses of 56 geomagnetic storms in the Afro-European sector (northern and southern hemispheres). They found that for most of the seasons, there were positive storm effects during the MP and that the negative storm effects were mainly observed at

high latitudes. In winter hemisphere, there were both positive and negative storm effects over the high latitudes. During the equinoxes, the storm-time TEC was not consistent with the summer distribution in the northern hemisphere.

A study by Yizengaw (2004) found negative storm effects over the Australian eastern region in the mid- and high latitudes and positive storm effects in the auroral and equatorial latitudes during a severe magnetic storm on 1999/09/22. Using TEC derrived from GPS satellite data and f_oF_2 derived from ionosondes, he found that the enhanced energy input to the ionosphere caused heating of the ionised and neutral gases and the disturbed thermospheric circulation which moved the plasma up and down along the magnetic field lines, changing the rate of production and recombination of the ionised species leading to the negative storm effect just after the SSC. Similarly, Fuller-Rowell *et al.* (1994) found that negative effects are caused by increases of molecular nitrogen in the regions of sunlight during the storm input, while the positive effects are caused by the decreases in mean molecular mass in regions of previous downwelling. TIDs induced by TADs caused by energy injection into the upper atmosphere could have participated in these storm effects creation during their propagations. Using the data from ground-based ionosondes, Prölss (1991) highlighted the causes of negative and positive ionospheric storm effects.

Figures A.1 - A.3 in Appendix A show responses of other storm days which are not shown in the results chapter. For the 14 storm days over 4 stations, 225 storm effects were found and examined. Of these storm effects, 8.9% were negative, 13.3% were positive and 77.8% were combination of both the negative and positive storm effects. Most of the storm effects were combinations of both the negative and positive storm effects, with 46.7% occurring during the MP and 41.3% occurring during the RP of these storms. 1.3% occurred during the IP, 0.9% during the IMP and 9.8% during the MRP. 3.5%, 36.5%, 31.5% and 28.5% of the storm effects occurred in summer, autumn, winter and spring, respectively.

4.1.4   Scintillation at SANAE station

Only 10 of the 14 storm periods studied here had sufficient scintillation data for analysis. All these storms were accompanied by strong phase and weak amplitude scintillations, except

that for two storm periods the amplitude scintillation increased slightly. Figure 4.6, in its top panel, shows that there was a significant enhancement of the phase scintillation during a strong storm on 2012/07/15 and it reached a maximum value of 1 radian. The duration of the phase scintillation enhancement was ∼32 hours and occurred during the MRP of the storm. The middle panel of Figure 4.6 shows that there was an increase in the amplitude
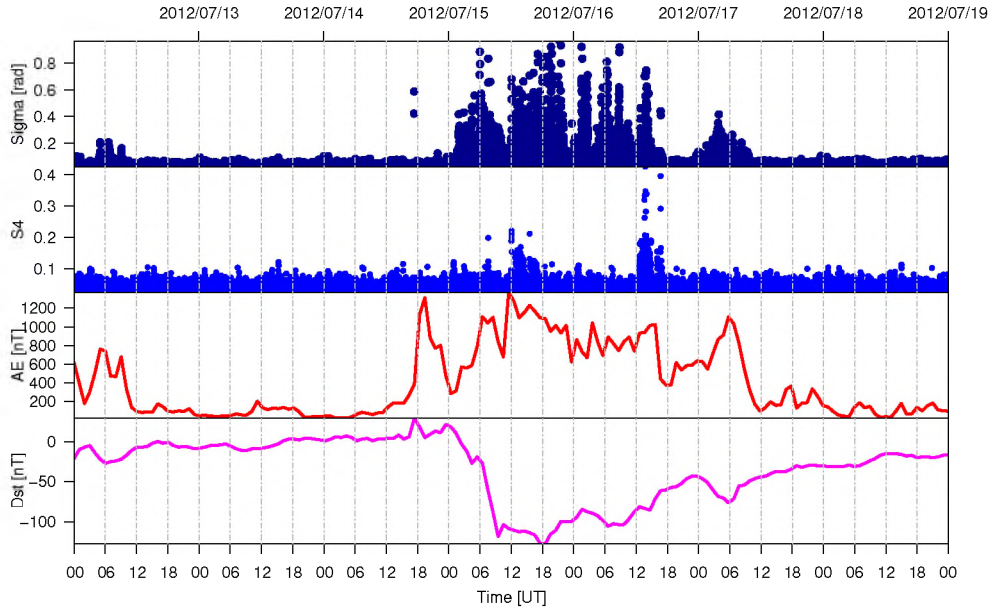
Figure 4.6: The phase and amplitude scintillation for 2012/07/15

scintillation to a maximum of ∼ 0.4, with a duration of about 6 hours, during the recovery phase of the storm. The durations were calculated as the period during which $\sigma_\phi > 0.3$ and $S_4 > 0.3$, during the storm periods. More phase and amplitude scintillation figures are found in Appendix B. Table 4.6 gives a summary of the phase and amplitude scintillation for the analysed storms. These results show that phase scintillation was at its maximum value of 1.0 rad for most of the storms (57.1%), except for the storms on 2011/10/25 and 2014/02/19. 14.3% of the storms caused the phase scintillation between 0.7 radians and 1 radian and there was no data for the remaining 28.6%. The amplitude scintillation increased to 0.4 on 2012/07/15 and to 0.42 on 2012/11/14. The duration of phase scintillations were estimated to vary between 6 and 32 hours, as shown in Table 4.6.

The causes of the phase scintillation during these storms are irregularities associated with large density gradients, storm enhancement density (SED), the enhancement of auroral pre-

Table 4.6: A table of the phase and amplitude scintillation, the storm phase during which it occurred and the duration at SANAE GPS station

Scintillation during geomagnetic storms			
Storm day	σ_ϕ (max) in rad & storm phases	S_4 (max) & storm phases	Duration of σ_ϕ (hours)
On 2011/09/27	1 during MRP	0.25 during MRP	12
On 2011/10/25	0.74 during MRP	0.25 during MRP	13
On 2012/03/09	1 during MRP	0.18 during MRP	15
On 2012/04/24	1 during MRP	0.14 during MRP	14
On 2012/07/15	1 during MRP	0.4 during RP	32
On 2012/10/01	1 during MRP	0.1 during MRP	6
On 2012/11/14	1 during MRP	0.42 during MP	9
On 2014/02/19	0.95 during MRP	0.22 during MRP	10
On 2015/03/17	1 during MRP	0.26 during MRP	20
On 2015/06/23	1 during MRP	0.25 during MRP	8

cipitation (as shown in the third panel of Figure 4.6) and the transported higher density plasma as reported by Wang *et al.* (2016). The enhancement of ionisation enters the polar cap in the form of a tongue and gives rise to the tongue of ionisation (TOI), which in turn leads to the phase scintillation, when the satellite signals pass through them. Similar effects (SED and TOI) were found for the 2011/09/27 and 2015/03/17 storms. These effects are discussed in the studies by Zhang *et al.* (2013) in the investigation of the evolution of polar cap ionisation patches, and Cherniak and Zakharenkova (2015), in a study of the high-latitude plasma irregularities in auroral activity indices. Another irregularity which may cause scintillation is polar cap patches, which are islands of high-density F_2 region ionospheric plasma, moving poleward of the auroral oval and surrounded by plasma of less density. This was reported by Zhang *et al.* (2013). Instabilities, such as the Kelvin-Helmholtz instability, gradient drift instability, soft electron precipitation and the current convective generated by the high-density gradient with different small-size irregularities, could be the cause of the amplitude scintillation (Weber *et al.*, 1986; Kersley *et al.*, 1988; De Franceschi *et al.*, 2008).

A study done by Mitchell *et al.* (2005) reported that both amplitude and phase scintillation coexisted in the strong gradients in TEC at the edge of polar cap patches near the nightside auroral oval during the Halloween storm of October 2003. Wang *et al.* (2016) compared large-scale irregularities and scintillations in the polar ionosphere during the geomagnetic storm of 2014/02/27 and found that the SED plume, the middle-latitude trough, and the polar cap

patches were the cause of irregularities. They also found that the phase scintillation was much larger than the amplitude scintillation associated with the burst flows or flow reversals at the equatorward edge of the middle-latitude trough in the post-noon sector and in the SED segmented area. Prikryl *et al.* (2015) studied the strong storm of 2012/03/09 using several instruments, including GPS, and found that the phase scintillation was associated with coupling processes between the solar wind and the magnetosphere-ionospheric system. In the nightside auroral oval, the strongest scintillation was caused by a combination of the large southward IMF and high solar wind dynamic pressure. There was also a correlation between this scintillation and the ground magnetic field perturbations and riometers absorption enhancements. The phase scintillation was collocated with mapped auroral emission and with ionospheric convection in the expanded dawn and dusk cells, with antisunward convection in the polar cap and with a TOI into the polar patches. Meeren *et al.* (2014) discussed on TOI stretched across the polar cap in the nightside ionosphere on 31st October 2011. In this study, they used GPS, all-sky imager, the European Incoherent Scatter Svalbord Radar and the SuperDARN data. The front of the TOI had between tens of meters and several kilometers. The bursts of phase scintillation were located to the TOI density gradient.

4.2   TIDs during geomagnetic storms

In order to investigate TIDs, vertical TEC (Vtec data) derived for individual PRNs (satellites) was used. The data are detrended using a one hour running mean in order to remove the diurnal trend and therefore obtain TID signatures denoted by dVtec [TECU]. The TIDs are also found in signatures of SuperDARN power, Doppler velocity and spectral width variations observed from ground backscatter (Grocott *et al.*, 2013). However, for most of our considered storm days, the power and the Doppler velocity were not available for the SuperDARN HF radars. The reasons of this unavailability could be:

- the equatorward shift of the auroral oval which is the main sink of ionospheric irregularities responsible for reflection of signals (Danilov and Lastovicka, 2001)

- absorption of signals in the lower part of the ionosphere

- and the absence (lack) of other mechanisms generating field-aligned irregularities in the

ionosphere.

The convection maps are used to show the plasma motions (flows) that may be associated with TIDs found during geomagnetic storms.

Instabilities may occur in the ionosphere when the medium is in an unstable equilibrium. Any external perturbation like solar wind pressure causes the decrease in potential energy of the fluid medium so that its oscillation or wave energy increases. Some of the instabilities take place when a stream of ions and electrons differ in velocity by more than the ion-acoustic speed (two-stream instability) or when the reduction of the total energy is caused by the interchange of two elements of a fluid (gradient drift instability) or between two media of relative motion (two boundaries with different velocities). All of these instabilities in the concerned medium may give rise to different types of waves. The high speed flows impart energy by Joule heating, the heat gradients send up instabilities in the plasma and these instability bursts could be the source of TIDs in the ionosphere.

4.2.1   TIDs signatures and convection maps

Figure 4.7(a) shows a TID structure detected by SANAE SuperDARN's beam 12 between 12:00 and 16:00 UT on 2012/07/15. This structure is suspected of having originated from a source that is equatorward of SANAE (i.e. a TID is travelling away from radar towards the pole), because beam 12 points towards the pole and the positive slopes of the power, Doppler velocity and spectral width of the signatures of TIDs, moving away from the radar. The top panel of Figure 4.7(b) shows a detailed power series during the main phase of the storm on 2012/07/15 which shows signatures of the detected TID. A similar TID was observed in TEC measurements of PRN 3 by a GPS receiver collocated with the radar (but not directly under the field-of-view), as shown by Figure 4.7 (c). Power spectra of these data sets (see bottom panels of Figure 4.7 (b) and (c)) show that the first peak is at roughly 0.32 mHz (i. e. its period is $\sim$ 52 minutes).

Most of the time, TIDs travel with speeds between 100 and 1000 ms^{-1} at high latitudes (Huang et $al.$, 1998; Fujiwara and Miyoshi, 2006), therefore one or two hours delay between the source and TIDs observed by the radar is to be expected if the source is suspected to be
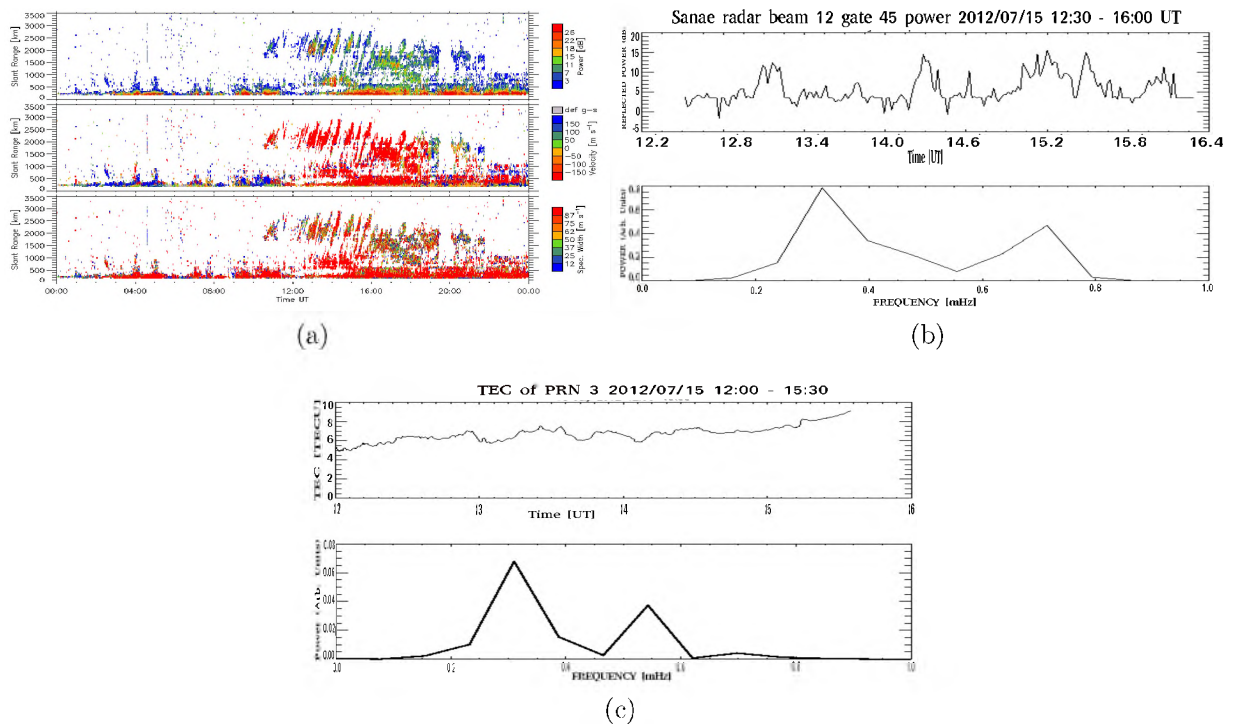
Figure 4.7: (a) The TIDs observed by the SuperDARN HF radar over SANAE station, (b) the power from SuperDARN and (c) TEC derived from GPS receiver of PRN 3 on 2012/07/15 storm day

out of the field-of-view region. In its constellation, PRN 3 observed the multiple wavefronts of a LSTID from around 11:40 UT until 15:30 UT as shown in the VTEC perturbation in Figure 4.8(a). The amplitude of this TID was 0.6 TECU. The convection map (in Figure 4.8(b) obtained from the Virginia Tech web-site (http://vt.superdarn.org/tiki-index.php)) shows a very high drift velocity of the plasma in the region, which would lead to Joule heating. The source region could be at a magnetic coordinate of around -70° latitude with a drift velocity of $\sim 600~ms^{-1}$ as measured by Kerguelen (KER) radar. It would therefore be reasonable to infer such high velocities also occurring just equatorward of Sanae. This would be associated with the electrojet, as it is an area associated on this map with the convection reversal boundary. In Figure 4.8(c) the two right-side panels show the Doppler velocities with the positive velocities (of $\sim 300~ms^{-1}$ in blue) and negative velocities ($\sim$ - $300~ms^{-1}$ in red) of the downward and upward ionospheric motions respectively. As suggested by Hayashi et al. (2010), the positive velocity implies downward (corresponding to TEC increase) and negative implies upward ionospheric motion (corresponding to TEC decrease). The left-hand panel of Figure 4.8(c) shows GPS TEC in which a density trough, which may be formed by

ionospheric expansion due to Joule heating in SuperDARNs' FOVs.

Figure 4.9(a) shows a TID of the amplitude $\sim$ 2 TECU measured by PRN 15 between 20:00 and 21:45 UT. Figure 4.9(b) (with the black closed lines) shows a convection map with higher plasma drift with a regions of high velocity above $\sim$ 600 ms^{-1}, which would give a Joule heating and generates the TID by means of instabilities. Figure 4.9(b) was downloaded from http://vt.superdarn.org/tiki-index.php. Figure 4.9(c) shows 4 panels. The two left panels show GPS TEC measurements where it is clear that there was a TOI in the southern polar region. The top right-hand panel shows the upward and downward motion with a velocity greater than $\sim \pm 500$ ms^{-1} in the ionosphere during a geomagnetic storm. The bottom right-hand panel shows the reflected power and GPS TEC of the polar ionosphere.

Only 11 of 14 storm periods studied had TID structures over SANAE. Table 4.7 reveals that an individual TID lasted between 1.7 and 5 hours, the amplitude varied from 0.2 to 5 TECU and its period varied from 17.5 to 52.3 minutes. 70.6% of the TIDs had amplitudes between 0.2 and 2 TECU, 29.4% had amplitudes between 2.1 and 5 TECU. Less than a half (47.1%) of the TIDs had periods between 17.5 and 29 minutes, while 52.9% had periods between 30 and 52.3 minutes. Finally, 11.8% , 64.7%, and 23.5% of the TIDs had a duration between 1.7 and 2 hours, 3 and 4 hours, and between 4.1 and 5 hours, respectively.

The TIDs at SANAE occurred during different seasons and had varying periods during these strong storms, as shown in Figure 4.10 and Table 4.7. This figure shows that 5.9%, 41.2%, 29.4% and 23.5% of TIDs occurred in summer, autumn, winter and spring respectively. Figure 4.10 and Table 4.7 show that all the TIDs have periods of less than 1 hour and the longest period was in autumn. The table also reveals that most of the TIDs ($\sim$ 64.7%) occurred prior to local sunrise and 35.7% occurred after local sunrise.

Large enhancement of the AE indices during intense storms (as can be seen in Appendix C (Figures C.1)) indicate injection of large amounts of energy into the auroral zone, which may lead to generation of TIDs via Joule heating, as discussed by Hocke and Schlegel (1996)

(a)

(b)   (c)

Figure 4.8: (a) The TID of PRN3, (b) the South Pole convection map and (c) the TEC, velocity and power of radars on 2012/07/15 storm day

and De Jesus *et al.* (2016). A similar study by Frissell *et al.* (2016) focused on MSTIDs observed during the winter daytime using HF in high latitudes and midlatitudes in Northern America between 2012 and 2015. They suggested that those TIDs occurred during periods of strong polar vortex and their sources could be space weather and lower atmospheric processes. Sofko and Huang (2000) studied the SuperDARN observations of medium-scale wave pairs generated by Joule heating in the auroral zone during the IMF B_z perturbation

Table 4.7: A table of parameters of TIDs at SANAE station

Parameters of TIDs				
Storm day	PRN	Amplitude (TECU)	Period (min)	Time (UT)
2011/08/06	15	0.2	17.5	00:40 - 04:00
2011/08/06	19	0.2	24	00:00 - 03:30
2011/09/27	2	5	52.3	15:30 - 18:50
2011/09/27	10	5	45.8	16:30 - 20:00
2011/10/25	25	2.5	25.4	00:00 - 04:30
2012/03/09	32	2	22.7	01:40 - 06:00
2012/04/24	4	3	41.5	00:30 - 03:30
2012/04/24	23	2	26.75	00:40 - 05:40
2012/07/15	3	0.6	52	11:40 - 15:30
2012/07/15	15	2	40.5	01:30 - 04:30
2012/07/15	18	0.6	30	01:00 - 04:00
2012/10/01	16	1.5	35.8	04:40 - 08:00
2012/10/01	31	2.5	31.4	01:00 - 04:50
2012/10/09	3	1.5	19.3	06:00 - 09:50
2012/11/14	28	2	25.1	06:30 - 08:30
2014/02/19	23	1	39.8	03:00 - 08:00
2015/03/17	15	2	21.1	20:00 - 21:45

which caused oscillations in the ionospheric electric field at the period of ~ 100 minutes in 1998/12/02. They found that each electric field enhancement could generate a pair of gravity waves by increasing Joule heating which, in turn, generated a pair of gravity waves. They also found that the duration of Joule heating events in their case were longer than those in the previous events, which was the reason for the two gravity wave pulses. Huang *et al.* (1998) published on observations of solar wind directly driven auroral electrojets and gravity waves. They found a cause-and-effect relationship between the IMF's southward turnings, the auroral electrojets, and the gravity waves. They also found a quasiperiodic occurrence of the gravity wave pulses which was determined by the repetitive energy input in the source region and concluded that " each burst of the auroral electrojet generated a single gravity wave pulse". Hayashi *et al.* (2010) studied LSTIDs observed by the SuperDARN Hokkaido HF radar and the GPS Earth Observation Network (GEONET) on 2006/12/15 and found a positive correlation between downward ionospheric motion and increasing TEC. They also found that two disturbances propagated southward and another disturbance propagated northward between 00:00 and 06:00 UT on 2006/12/15. Another similar study was done by Karpachev *et al.* (2010), who detected two LSTIDs associated with the dayside cusp. They used Super-

(a)

(b)   (c)
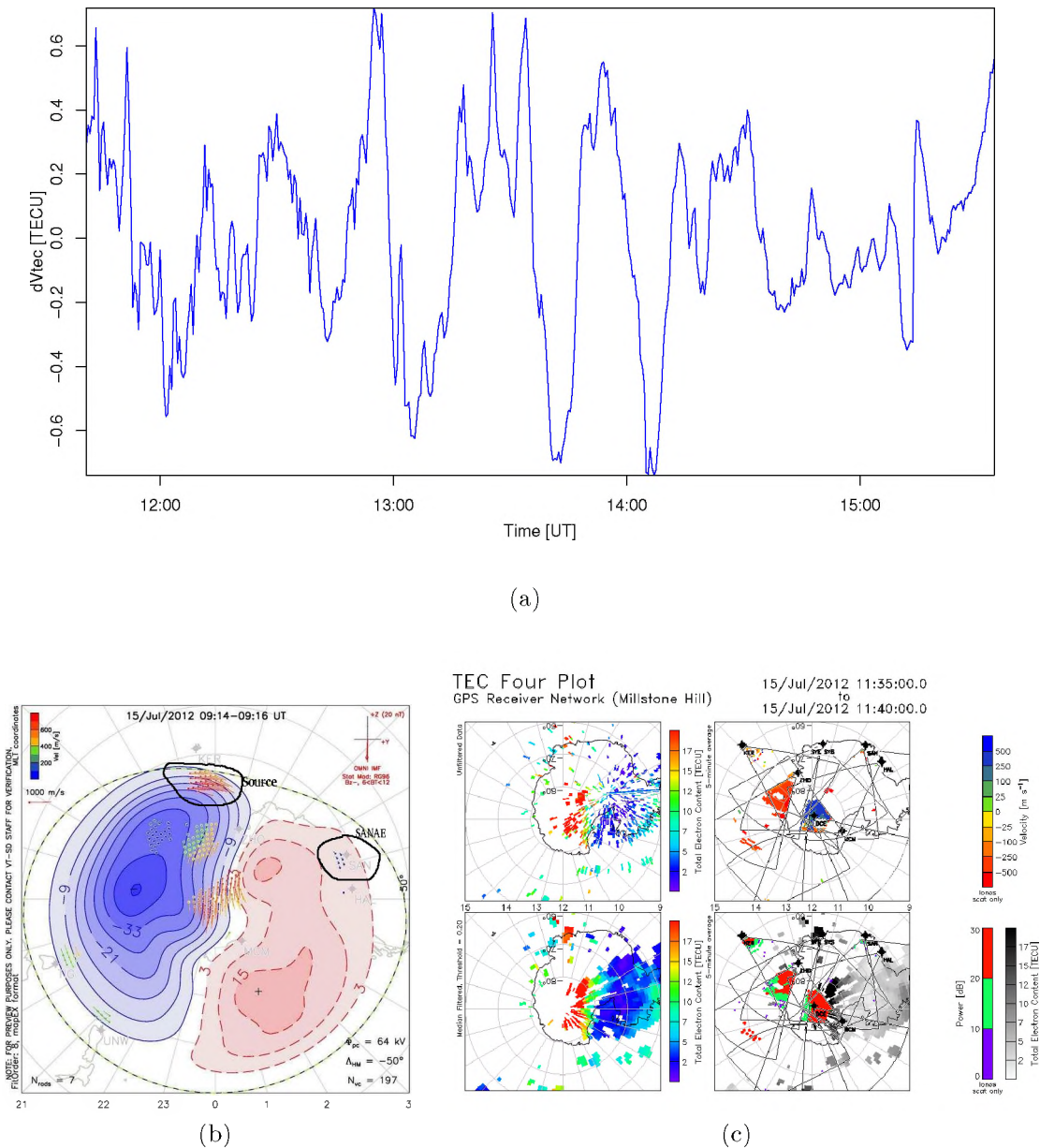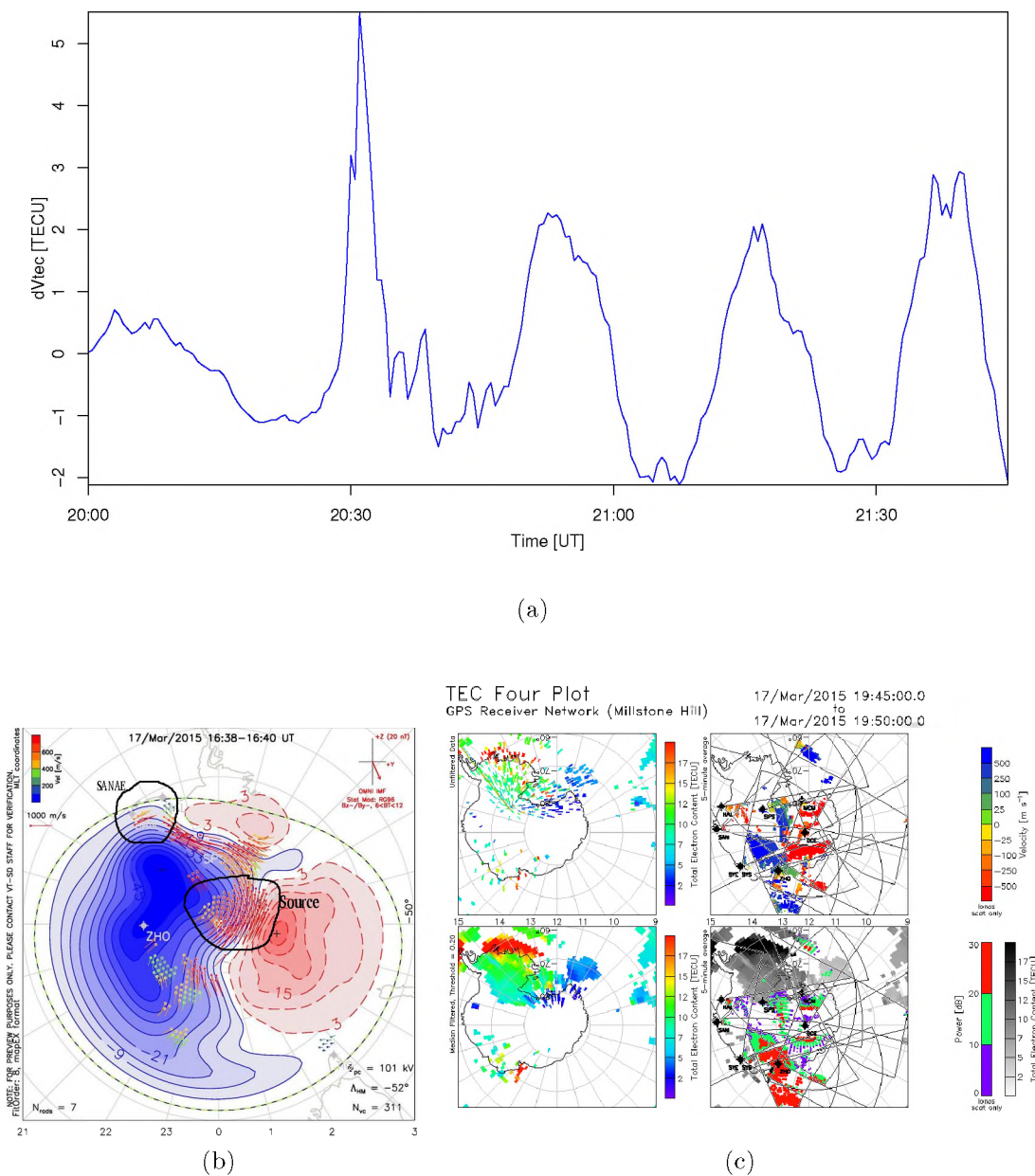
Figure 4.9: (a) The TID of PRN 15, (b) the South Pole convection map and (c) TEC, velocity and power of radars on 2015/03/17 storm day.

DARN data for the 1998/02/17 substorm, which originated from plasma convection. The LSTIDs had wave periods of 1.5 and 2 hours, a velocity of $\sim 400\ ms^{-1}$ for both wave periods and wavelengths of 2200 and 2900 km, respectively. They used a number of datasets, such as high-latitude convection maps, data from 4 DMSP satellites and from networks of ground-based magnetometers. Grocott *et al.* (2013), using SuperDARN HF radar (in which TIDs manifest as structured enhancements in echo power), showed that over the Peninsula in
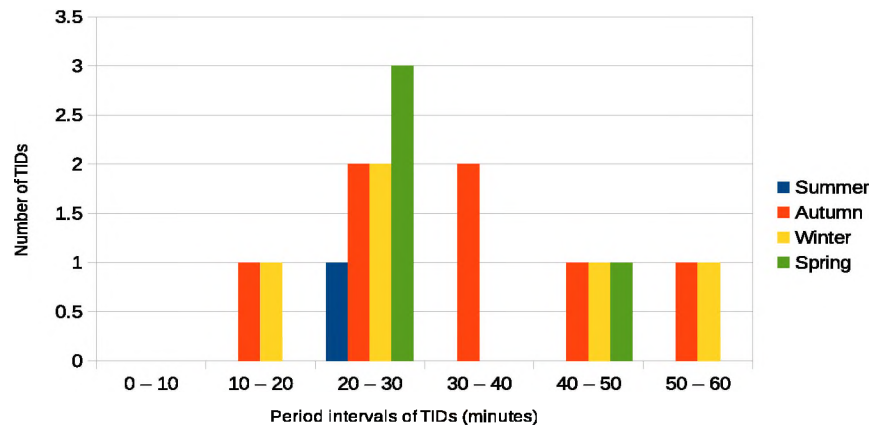
Figure 4.10: The periods of TIDs and their seasonal occurrence over SANAE station

Antarctica between May 2010 and April 2011, TIDs had periods between 30 and 80 minutes and speeds between 100 and 300 ms^{-1}. They concluded that these TIDs were MSTIDs and that they were caused by the "enhanced solar wind - magnetosphere coupling and a smaller, westward propagating population, that could be associated with atmospheric gravity waves excited by winds over the Andean and Antarctic Peninsula mountains or by the high winds of the Antarctic Polar Vortex". The ranges of TID periods presented in this study agree with the ranges of periods of TIDs of similar studies. This study corroborates the existence of these mechanisms.

4.3   Summary

During strong and severe (intense) magnetic storms, the ionospheric region over SANAE and its surroundings experienced the negative, positive and combinations of the two storm effects during IP, MP, IMP, MRP and RP between 2011 and 2015. The mechanisms that cause the depletion, enhancement and the simultaneous increase and decrease of electron concentrations in these regions were discussed. Phase and amplitude scintillation at SANAE show the appearance of large-scale irregularities for all considered storm days. Some parameters of TIDs and their associated mechanisms in the Antarctic ionosphere were discussed. The next chapter concludes the discussion of findings and proposes future work for a better understanding of high-latitude ionospheric responses.

Chapter 5

Conclusions and future work

5.1   Conclusions

The aim of this study was to investigate the responses of the ionosphere associated with geomagnetic storms with a minimum Dst of -100 nT, between 2011 and 2015 in the ionosphere over Antarctica. The study was conducted using GPS TEC, scintillation data and SuperDARN HF radar data. Storm effects expressed as the percentages of $dVtec$ were estimated by comparing $Vtec$ of a storm day and 28-day running median of $Vtec$. The storm effects were divided into three categories: negative storm effects, positive storm effects and a combination of both negative and positive storm effects. All storm days over 4 stations (Mawson, O'Higgins2, Syowa and SANAE) were identified and 225 storm effects were found. 8.9% of the storm effects were negative, 13.3% of the storm effects were positive and 77.8% were combination (of negative and positive) storm effects, i.e majority were a combination of positive and negative. Storm effects were most frequently observed during the main phase (46.7%) and recovery phase (41.3%). This study indicates that particle precipitation and enhancement of Joule heating during the storm events studied in this region played an important role in causing these storm effects.

Phase and amplitude scintillation data analysis showed that 57.1% of the 14 geomagnetic storms studied caused phase scintillation of 1 radian, while 14.3% caused phase scintillation between 0.7 and 1 radian. There was no data for the remaing 28.6%. The phase scintillation events lasted between 6 and 32 hours. 57.1% of the events did not have significant amplitude scintillation (i.e. their amplitude scintillation were below 0.3), while 14.3% had amplitude scintillations near 0.4. The amplitude scintillation events lasted between 2 and 6

hours. Irregularities associated with large density gradients, SED, the enhancement of auroral precipitations, the transported higher density plasma and TOI caused by the enhancement of ionization, are considered to be the major causes of scintillation in high-latitude regions (Zhang *et al.*, 2013; Cherniak and Zakharenkova, 2015).

TID signatures denoted by *dVtec* were identified by detrending *Vtec* derived from individual PRNs and from the SuperDARN power, Doppler velocity and spectral width variations. The FFT method was used to complete the periods of these TIDs observed over SANAE. Several storm-generated TIDs were observed in different seasons, with the majority of them (41.2%) occurring in autumn, and the minority (5.9%) in summer. The duration of these TIDs were between 1.7 and 5 hours, their amplitude varied between 0.2 and 5 TECU and their periods were between 17.5 and 52.3 minutes. During the storm of 2012/07/15 GPS and SuperDARN observed a similar TID of amplitude of 0.6 TECU and a period of 52 minutes. The source of this TID was identified to be within the plasma flowing at about 600 ms^{-1} on 2012/07/15 from 09:14 to 09:16 UT.

For most of the storms investigated here, auroral electrojet (AE) indices showed evidence of high energy injection, where AE values were above 1000 nT for extended periods. Super-DARN power, Doppler velocity and convection maps, as well as GPS TEC plots, revealed evidence of Joule heating as well as vertical motion of the ionosphere in the southern polar region. Therefore, it is postulated that TIDs were caused by energy injection in the high-latitude region (southern region), causing Joule heating and different kinds of instabilities during high-velocity flows of plasma.

5.2 Future work

This study was focused on the response of the ionosphere to the geomagnetic storms over SANAE and surroundings by using data from GPS, SuperDARN as well as Dst and AE to show the magnetic field disturbances. This study can be extended to cover the whole Antarctica using data from more GPS stations, SuperDARN radars, riometers, ionosondes, magnetometers and other instruments. This will enable us to gather more information on

TIDs (such as speeds, velocities and wavelengths) and regional scintillation. A comparison of responses in the southern and northern polar regions over a solar cycle or more should lead to a better understanding of the high-latitude response to geomagnetic disturbances and the dynamics involved.

5.3   Summary of the main observations

The summary of the main observations of this study is presented below as follow:

- 77.8% of the storm effects observed were a combination of negative and positive

- 8.9% of the storm effects were negative and mostly observed during the main phase of a storm

- 13.3% of the storm effects were positive and mostly observed during the recovery phase of a storm

- 71.4% of the 14 geomagnetic storms studied caused phase scintillation above 0.7 radians

- 14.3% of the 14 storms studied had a maximum amplitude scintillation of ~ 0.4

- Majority of TIDs (41.2%) occurred in autumn

- Minority of TIDs (5.9%) occurred in summer

- The durations of these TIDs were between 1.7 and 5 hours

- The periods of these TIDs were between 17.5 and 52.3 minutes

- The amplitudes of these TIDs were between 0.2 and 5 TECU

References

Adimula, I., Oladipo, O., and Adebiyi, S.: Latitudinal and Seasonal Investigations of Storm-Time TEC Variation, Pure and Applied Geophysics, pp. 1–13, 2016.

Axford, W.: The interaction between the solar wind and the earth's magnetosphere, Journal of Geophysical Research, 67, 3791–3796, 1962.

Balan, N., Otsuka, Y., Nishioka, M., Liu, J., and Bailey, G.: Physical mechanisms of the ionospheric storms at equatorial and higher latitudes during the recovery phase of geomagnetic storms, Journal of Geophysical Research: Space Physics, 118, 2660–2669, 2013.

Basu, S., Kudeki, E., Basu, S., Valladares, C., Weber, E., Zengingonul, H., Bhattacharyya, S., Sheehan, R., Meriwether, J., Biondi, M., et al.: Scintillations, plasma drifts, and neutral winds in the equatorial ionosphere after sunset, Journal of Geophysical Research: Space Physics, 101, 26 795–26 809, 1996.

Basu, Sunanda, S., McClure, J., Hanson, W., and Whitney, H.: High resolution topside in situ data of electron densities and VHF/GHz scintillations in the equatorial region, Journal of Geophysical Research: Space Physics, 88, 403–415, 1983.

Bernhardt, P. A., Siefring, C. L., Galysh, I. J., Rodilosso, T. F., Koch, D. E., MacDonald, T. L., Wilkens, M. R., and Landis, G. P.: Ionospheric applications of the scintillation and tomography receiver in space (CITRIS) mission when used with the DORIS radio beacon network, Journal of Geodesy, 80, 473–485, 2006.

Bristow, W. and Greenwald, R.: On the spectrum of thermospheric gravity waves observed by the Super Dual Auroral Radar Network, Journal of Geophysical Research: Space Physics, 102, 11 585–11 595, 1997.

Bristow, W., Greenwald, R., and Samson, J.: Identification of high-latitude acoustic gravity wave sources using the Goose Bay HF radar, Journal of Geophysical Research: Space Physics, 99, 319–331, 1994.

Buffett, B. A.: Earth's core and the geodynamo, Science, 288, 2007–2012, 2000.

Buresova, D. and Lastovicka, J.: Pre-storm electron density enhancements at middle latitudes, Journal of Atmospheric and Solar-Terrestrial Physics, 70, 1848–1855, 2008.

Burns, A., Solomon, S., Wang, W., and Killeen, T.: The ionospheric and thermospheric response to CMEs: Challenges and successes, Journal of Atmospheric and Solar-Terrestrial Physics, 69, 77–85, 2007.

Campbell, W. H.: Introduction to geomagnetic fields, Cambridge University Press, 2003.

Carrano, C. S., Groves, K. M., and Griffin, J. M.: Empirical characterization and modeling of GPS positioning errors due to ionospheric scintillation, in: Proceedings of the Ionospheric Effects Symposium, Alexandria, VA, 2005.

C.H, L.: World ionosphere/Thermosphere study, ICSU-SCOSTEP, 1989.

Chavalier, C.: The Earth's electrical surface potential: A summary of present understanding, California Institute for Human Science, Encinitas, CA, PhD, 2007.

Chen Francis, F.: Introduction to plasma physics, Springer, 1974.

Cherniak, I. and Zakharenkova, I.: Dependence of the high-latitude plasma irregularities on the auroral activity indices: a case study of 17 March 2015 geomagnetic storm, Earth, Planets and Space, 67, 1, 2015.

Cherniak, I., Zakharenkova, I., and Redmon, R. J.: Dynamics of the high-latitude ionospheric irregularities during the 17 March 2015 St. Patrick's Day storm: Ground-based GPS measurements, Space Weather, 13, 585–597, 2015.

Chisham, G., Lester, M., Milan, S. E., Freeman, M., Bristow, W., Grocott, A., McWilliams, K., Ruohoniemi, J., Yeoman, T. K., Dyson, P. L., *et al.*: A decade of the Super Dual Auroral Radar Network (SuperDARN): Scientific achievements, new techniques and future directions, Surveys in Geophysics, 28, 33–109, 2007.

Danilov, A. and Lastovicka, J.: Effects of geomagnetic storms on the ionosphere and atmosphere, International Journal of Geomagnetism and Aeronomy, 2, 209–224, 2001.

Davies, K.: Ionospheric radio, IET, 1990a.

Davies, K.: Ionospheric radio, IET, 1990b.

De Abreu, A., Fagundes, P., Sahai, Y., de Jesus, R., Bittencourt, J., Brunini, C., Gende, M., Pillat, V., Lima, W., Abalde, J., *et al.*: Hemispheric asymmetries in the ionospheric response observed in the American sector during an intense geomagnetic storm, Journal of Geophysical Research: Space Physics, 115, A12 312, 2010a.

De Abreu, A., Fagundes, P., Sahai, Y., de Jesus, R., Bittencourt, J., Brunini, C., Gende, M., Pillat, V., Lima, W., Abalde, J., *et al.*: Hemispheric asymmetries in the ionospheric response observed in the American sector during an intense geomagnetic storm, Journal of Geophysical Research: Space Physics, 115, A12 312, 2010b.

De Franceschi, G., Alfonsi, L., Romano, V., Aquino, M., Dodson, A., Mitchell, C. N., Spencer, P., and Wernik, A. W.: Dynamics of high-latitude patches and associated small-scale irregularities during the October and November 2003 storms, Journal of Atmospheric and Solar-Terrestrial Physics, 70, 879–888, 2008.

De Jesus, R., Fagundes, P., Coster, A., Bolaji, O., Sobral, J., Batista, I., de Abreu, A., Venkatesh, K., Gende, M., Abalde, J., *et al.*: Effects of the intense geomagnetic storm of September-October 2012 on the equatorial, low- and mid-latitude F region in the American and African sector during the unusual 24th solar cycle, Journal of Atmospheric and Solar-Terrestrial Physics, 138, 93–105, 2016.

Ding, F., Wan, W., Liu, L., Afraimovich, E., Voeykov, S., and Perevalova, N.: A statistical study of large-scale traveling ionospheric disturbances observed by GPS TEC during major magnetic storms over the years 2003–2005, Journal of Geophysical Research: Space Physics, 113, A00A01, 2008.

Ding, F., Wan, W., Ning, B., Zhao, B., Li, Q., Wang, Y., Hu, L., Zhang, R., and Xiong, B.: Observations of poleward-propagating large-scale traveling ionospheric disturbances in southern China, Annales Geophysicae, 31, 377–385, 2013.

Dubey, S., Wahi, R., and Gwal, A.: Ionospheric effects on GPS positioning, Advances in Space Research, 38, 2478–2484, 2006.

El-Rabbany, A.: Introduction to GPS: the Global Positioning System, Artech House, 2002.

Esposito, G.: Study of cosmic ray fluxes in Low Earth Orbit observed with the AMS experiment, Universita Degli di Perugia, Dottorato di Ricerca in Fisica, PhD, 2003.

Feldstein, Y. I. and Levitin, A.: Solar wind control of electric fields and currents in the ionosphere., Journal of Geomagnetism and Geoelectricity, 38, 1143–1182, 1986.

Ferraro, V.: On the theory of the first phase of a geomagnetic storm: A new illustrative calculation based on an idealised (plane not cylindrical) model field distribution, Journal of Geophysical Research, 57, 15–49, 1952.

Foster, J. and Rich, F.: Prompt midlatitude electric field effects during severe geomagnetic storms, Journal of Geophysical Research: Space Physics, 103, 26 367–26 372, 1998.

Frissell, N., Baker, J., Ruohoniemi, J., Greenwald, R., Gerrard, A., Miller, E., and West, M.: Sources and characteristics of medium-scale traveling ionospheric disturbances observed by high-frequency radars in the North American sector, Journal of Geophysical Research: Space Physics, 121, 3722–3739, 2016.

Fujiwara, H. and Miyoshi, Y.: Characteristics of the large-scale traveling atmospheric disturbances during geomagnetically quiet and disturbed periods simulated by a whole atmosphere general circulation model, Geophysical research letters, 33, 2006.

Fuller-Rowell, T., Codrescu, M., Moffett, R., and Quegan, S.: Response of the thermosphere and ionosphere to geomagnetic storms, Journal of Geophysical Research: Space Physics, 99, 3893–3914, 1994.

Gonzalez, W., Joselyn, J., Kamide, Y., Kroehl, H., Rostoker, G., Tsurutani, B., and Vasyliunas, V.: What is a geomagnetic storm?, Journal of Geophysical Research: Space Physics, 99, 5771–5792, 1994.

Greenwald, R. A., Oksavik, K., Erickson, P. J., Lind, F. D., Ruohoniemi, J. M., Baker, J. B., and Gjerloev, J. W.: Identification of the temperature gradient instability as the source of decameter-scale ionospheric irregularities on plasmapause field lines, Geophysical research letters, 33, 2006.

Grocott, A., Hosokawa, K., Ishida, T., Lester, M., Milan, S., Freeman, M., Sato, N., and Yukimatu, A.: Characteristics of medium-scale traveling ionospheric disturbances observed near the Antarctic Peninsula by HF radar, Journal of Geophysical Research: Space Physics, 118, 5830–5841, 2013.

Habarulema, J. B., Katamzi, Z. T., and Yizengaw, E.: First observations of poleward large-scale traveling ionospheric disturbances over the African sector during geomagnetic storm conditions, Journal of Geophysical Research: Space Physics, 120, 6914–6929, 2015.

Hargreaves, J.: The solar-terrestrial environment, Cambridge University Press, 1992.

Hargreaves, J.: Books-Received-the Solar-Terrestrial Environment-an Introduction to Geospace-the Science of the Terrestrial Upper Atmosphere Ionosphere and Magnetosphere, Science, 270, 652, 1995.

Hayashi, H., Nishitani, N., Ogawa, T., Otsuka, Y., Tsugawa, T., Hosokawa, K., and Saito, A.: Large-scale traveling ionospheric disturbance observed by SuperDARN Hokkaido HF radar and GPS networks on 15 December 2006, Journal of Geophysical Research: Space Physics, 115, A06 309, 2010.

Hocke, K. and Schlegel, K.: A review of atmospheric gravity waves and travelling ionospheric disturbances, Annales Geophysicae, 14, 917, 1996.

Hopkins, J.: GUVI Global Ultraviolet Imager, `http://guvi.jhuapl.edu/site/gallery/guvi-gallery13on2.shtml`, [Online; accessed 2016/09/06], 2016.

Horvath, I.: Impact of 10 January 1997 geomagnetic storm on the nighttime Weddell Sea Anomaly: A study utilizing data provided by the TOPEX/Poseidon mission and the Defense Meteorological Satellite Program, and simulations generated by the Coupled Thermosphere/Ionosphere Plasmasphere model, Journal of Geophysical Research: Space Physics, 112, A06 329, 2007.

Horvath, I. and Lovell, B. C.: Positive and negative ionospheric storms occurring during the 15 May 2005 geomagnetic superstorm, Journal of Geophysical Research: Space Physics, 120, 7822–7837, 2015.

Huang, C.-S., Andre, D. A., and Sofko, G. J.: Observations of solar wind directly driven auroral electrojets and gravity waves, Journal of Geophysical Research: Space Physics, 103, 23 347–23 356, 1998.

Huang, C.-S., Sofko, G., Kustov, A., MacDougall, J., Andre, D., Hughes, W., and Papitashvili, V.: Quasi-periodic ionospheric disturbances with a 40-min period during prolonged northward interplanetary magnetic field, Geophysical research letters, 27, 1795–1798, 2000.

Huang, C.-S., Foster, J., Goncharenko, L., Erickson, P., Rideout, W., and Coster, A.: A strong positive phase of ionospheric storms observed by the Millstone Hill incoherent scatter radar and global GPS network, Journal of Geophysical Research: Space Physics, 110, A06 303, 2005.

Hunsucker, R. D.: Atmospheric gravity waves generated in the high-latitude ionosphere, Reviews of Geophysics, 20, 293–315, 1982.

Hunsucker, R. D. and Hargreaves, J. K.: The high-latitude ionosphere and its effects on radio propagation, Cambridge University Press, 2007.

Idrus, I. I., Abdullah, M., Hasbi, A. M., Husin, A., and Yatim, B.: Large-scale traveling ionospheric disturbances observed using GPS receivers over high-latitude and equatorial regions, Journal of Atmospheric and Solar-Terrestrial Physics, 102, 321–328, 2013.

Iyer, C. and Prabhu, G.: Moving signals and their measured frequencies, arXiv preprint arXiv:1201.3205, 2, 24–36, 2013.

Jerri, A. J.: The Gibbs phenomenon in Fourier analysis, splines and wavelet approximations, vol. 446, Springer Science & Business Media, 2013.

Jin, R., Jin, S., and Tao, X.: Ionospheric anomalies during the March 2013 geomagnetic storm from BeiDou navigation satellite system (BDS) observations, in: China Satellite Navigation Conference (CSNC) 2014 Proceedings: Volume I, pp. 97–104, Springer, 2014.

John, V. D. A.: Satellite navigation science and technology for Africa, The Abdus Salam, International Center for Theoretical Physics, 2007.

Jursa, A. S. *et al.*: Handbook of Geophysics and the Space Environment, Air Force Geophysics Laboratory, Air Force Systems Command, United States Air Force, 1985.

Kamide, Y. and Baumjohann, W.: Magnetosphere-ionosphere coupling, Springer Science & Business Media, 1993.

Kantor, I., de Paula, E., and de Rezende, L.: TEC Measurements with GPS data, INPE-Aeronomy Division, Sao Paulo, Brasil, 2006.

Kaplan, E. and Hegarty, C.: Understanding GPS: Principles and applications, Artech house, 2005.

Karpachev, A., Beloff, N., Carozzi, T., Denisenko, P., Karhunen, T., and Lester, M.: Detection of large scale TIDs associated with the dayside cusp using SuperDARN data, Journal of Atmospheric and Solar-Terrestrial Physics, 72, 653–661, 2010.

Kathryn McWilliams, Dieter Andre, R. G. A. S. G. S. T. Y.: SuperDARN pulse sequences: Optimisation and testing, in: SuperDARN workshop, Finland, 2003.

Kelley, M. C.: The Earth's Ionosphere: Plasma Physics and Electrodynamics, Academic press, 2009.

Kennel, C. F.: Convection and Substorms - Paradigms of magnetospheric phenomenology, Oxford University Press, 2, 432, 1996.

Kersley, L., Pryse, S., and Wheadon, N.: Amplitude and phase scintillation at high latitudes over northern Europe, Radio Science, 23, 320–330, 1988.

Kikuchi, T., Liihr, H., Schlegel, K., Tachihara, H., and Shinohara, M.: Penetration of auroral electric fields to the equator, Journal of geophysical research, 105, 23 251–23 261, 2000.

Kintner, P., Ledvina, B., and De Paula, E.: GPS and ionospheric scintillations, Space Weather, 5, S09 003, 2007.

Klimenko, M., Klimenko, V., Karpachev, A., Ratovsky, K., and Stepanov, A.: Spatial features of Weddell Sea and Yakutsk Anomalies in foF2 diurnal variations during high solar

activity periods: Interkosmos-19 satellite and ground-based ionosonde observations, IRI reproduction and GSM TIP model simulation, Advances in Space Research, 55, 2020–2032, 2015.

Kyoto: World Data Center for Geomagnetism, `http://wdc.kugi.kyoto-u.ac.jp/`, [Online; accessed 2015/07/22], 2015.

Kyoto: Geomagnetic elements, `http://wdc.kugi.kyoto-u.ac.jp/element/eleexp.html`, [Online; accessed 2016/03/18], 2016.

Lakhina, G. S. and Tsurutani, B. T.: Magnetic storms and electromagnetic pulsations, in: Encyclopedia of Solid Earth Geophysics, by Harsh.K. Gupta, pp. 792–796, Springer, 2011.

Leadon, R., Woods, A., Wenaas, E., and Klein, H.: Analytical Investigation of Emitting Probes in an Ionized Plasma., Tech. rep., DTIC Document, 1981.

Lester, M.: The Super Dual Auroral Radar Network SuperDARN: an overview of its development and science, Advances in Polar Science, 24, 1–11, 2013.

Loewe, C. and Prölss, G.: Classification and mean behavior of magnetic storms, Journal of Geophysical Research: Space Physics, 102, 14 209–14 213, 1997.

Loudet, L.: SID Monitoring station, `http://sidstation.loudet.org/ionosphere-en.xhtml`, [Online; accessed 2016/05/05], 2016.

Lu, G., Richmond, A., Roble, R., and Emery, B.: Coexistence of ionospheric positive and negative storm phases under northern winter conditions: A case study, Journal of Geophysical Research: Space Physics, 106, 24 493–24 504, 2001.

Matamba, T. M., Habarulema, J. B., and McKinnell, L.-A.: Statistical analysis of the ionospheric response during geomagnetic storm conditions over South Africa using ionosonde and GPS data, Space Weather, 13, 536–547, 2015.

Matsuo, T. and Richmond, A.: SuperDARN assimilative mapping, Journal of Geophysical Research: Space Physics, 118, 7954–7962, 2013.

McHarg, M., Chun, F., Knipp, D., Lu, G., Emery, B., and Ridley, A.: High-latitude Joule heating response to IMF inputs, Journal of Geophysical Research: Space Physics, 110, A08 309, 2005.

McNamara, L. F.: The Ionosphere: Communications, Surveillance, and Direction Finding, Krieger, 1991.

Meeren, C., Oksavik, K., Lorentzen, D., Moen, J. I., and Romano, V.: GPS scintillation and irregularities at the front of an ionization tongue in the nightside polar ionosphere, Journal of Geophysical Research: Space Physics, 119, 8624–8636, 2014.

Mikhailov, A., Skoblin, M., and Forster, M.: Daytime F2-layer positive storm effect at middle and lower latitudes, in: Annales Geophysicae, vol. 13, p. 532, 1995.

Mio: History of GPS, http://www.mio.com/tecnology-history-of-gps.htm, [Online; accessed 2016/04/05], 2016.

Mitchell, C. N., Alfonsi, L., De Franceschi, G., Lester, M., Romano, V., and Wernik, A.: GPS TEC and scintillation measurements from the polar ionosphere during the October 2003 storm, Geophysical Research Letters, 32, 2005.

NASA: Stereo catalog, http://ccmc.gsfc.nasa.gov/analysis/stereo/, [Online; accessed 2016/03/21], 2016.

Oinats, A. V., Kurkin, V. I., and Nishitani, N.: Statistical study of medium-scale traveling ionospheric disturbances using SuperDARN Hokkaido ground backscatter data for 2011, Earth, Planets and Space, 67, 1–9, 2015.

Otsuka, Y., Shiokawa, K., and Ogawa, T.: Equatorial ionospheric scintillations and zonal irregularity drifts observed with closely-spaced GPS receivers in Indonesia, Journal of the Meteorological Society of Japan. Ser. II, 84, 343–351, 2006.

Palmroth, M., Janhunen, P., Pulkkinen, T., Aksnes, A., Lu, G., Østgaard, N., Watermann, J., Reeves, G., and Germany, G.: Assessment of ionospheric Joule heating by GUMICS-4 MHD simulation, AMIE, and satellite-based statistics: towards a synthesis, in: Annales Geophysicae, vol. 23, pp. 2051–2068, 2005.

Pi, X., Mannucci, A., Lindqwister, U., and Ho, C.: Monitoring of global ionospheric irregularities using the worldwide GPS network, Geophysical Research Letters, 24, 2283–2286, 1997.

Prikryl, P., Ghoddousi-Fard, R., Thomas, E., Ruohoniemi, J., Shepherd, S., Jayachandran, P., Danskin, D., Spanswick, E., Zhang, Y., Jiao, Y., *et al.*: GPS phase scintillation at high latitudes during geomagnetic storms of 7–17 March 2012–Part 1: The North American sector, Ann. Geophys, 33, 637–656, 2015.

Prölss, G.: Thermosphere-ionosphere coupling during disturbed conditions, Journal of geomagnetism and geoelectricity, 43, 537–549, 1991.

Prölss, G., Roemer, M., and Slowey, J.: Dissipation of solar wind energy in the Earth's upper atmosphere: The geomagnetic activity effect, Advances in space research, 8, 215–261, 1988.

Prölss, G. W.: Ionospheric F-region storms, Handbook of Atmospheric Electrodynamics, 2, 195–248, 1995.

Ribeiro, A., Ruohoniemi, J., Ponomarenko, P., N Clausen, L., H Baker, J., Greenwald, R., Oksavik, K., and Larquier, S.: A comparison of SuperDARN ACF fitting methods, Radio Science, 48, 274–282, 2013.

Rodriguez-Bouza, M., Herraiz, M., Rodríguez-Caderot, G., Paparini, C., Otero, X., and Radicella, S. M.: Comparison between the effect of two geomagnetic storms with the same seasonal and daily characteristics and different intensity on the European ionosphere., in: EGU General Assembly Conference Abstracts, vol. 18, p. 12574, 2016.

Sakuraba, A. and Roberts, P. H.: Generation of a strong magnetic field using uniform heat flux at the surface of the core, Nature Geoscience, 2, 802–805, 2009.

Salah, J. and Holt, J.: Midlatitude thermospheric winds from incoherent scatter radar and theory, Radio Science, 9, 301–313, 1974.

Samson, J., Greenwald, R., Ruohoniemi, J., and Baker, K.: High-frequency radar observations of atmospheric gravity waves in the high-latitude ionosphere, Geophysical Research Letters, 16, 875–878, 1989.

Savage, B. D. and Sembach, K. R.: Interstellar abundances from absorption-line observations with the Hubble Space Telescope, Annual Review of Astronomy and Astrophysics, 34, 279–329, 1996.

Shepherd, S.: A dynamical model of high-latitude convection derived from SuperDARN plasma drift measurements, Journal of Geophysical Research: Space Physics, 115, A12329, 2010.

Shreedevi, P., Thampi, S. V., Chakrabarty, D., Choudhary, R., Pant, T. K., Bhardwaj, A., and Mukherjee, S.: On the latitudinal changes in ionospheric electrodynamics and composition based on observations over the 76–77° E meridian from both hemispheres during a geomagnetic storm, Journal of Geophysical Research: Space Physics, 2016.

Sofko, G. J. and Huang, C.-S.: SuperDARN observations of medium-scale gravity wave pairs generated by Joule heating in the auroral zone, Geophysical research letters, 27, 485–488, 2000.

Sreeja, V. V., Aquino, M., Forte, B., Elmas, Z., Hancock, C., De Franceschi, G., Alfonsi, L., Spogli, L., Romano, V., Bougard, B., *et al.*: Tackling ionospheric scintillation threat to GNSS in Latin America, Journal of Space Weather and Space Climate, 1, A05, 2011.

Steme, K. T., Greenwald, R. A., Baker, J. B., and Ruohoniemi, J. M.: Modeling of a twin terminated folded dipole antenna for the Super Dual Auroral Radar Network SuperDARN, in: Radar Conference (RADAR), pp. 934–938, IEEE, 2011.

Stern, D. P.: A brief history of magnetospheric physics during the space age, Reviews of Geophysics, 34, 1–31, 1996.

Stolle, C., Manoj, C., Lühr, H., Maus, S., and Alken, P.: Estimating the daytime equatorial ionization anomaly strength from electric field proxies, Journal of Geophysical Research: Space Physics, 113, A09310, 2008.

Susumu, K.: Middle atmosphere research and radar observation, Proceedings of the Japan Academy, Series B, 81, 306–320, 2005.

Thomas, E., Baker, J. B., Ruohoniemi, J. M., Clausen, L. B., Coster, A., Foster, J., and Erickson, P.: Direct observations of the role of convection electric field in the formation of

a polar tongue of ionization from storm enhanced density, Journal of Geophysical Research: Space Physics, 118, 1180–1189, 2013.

Titheridge, J.: Large-scale irregularities in the ionosphere, Journal of Geophysical Research, 68, 3399–3417, 1963.

Tsagouri, I., Belehaki, A., Moraitis, G., and Mavromichalaki, H.: Positive and negative ionospheric disturbances at middle latitudes during geomagnetic storms, Geophysical Research Letters, 27, 3579–3582, 2000.

Tsugawa, T., Saito, A., and Otsuka, Y.: A statistical study of large-scale traveling ionospheric disturbances using the GPS network in Japan, Journal of Geophysical Research: Space Physics, 109, A06 302, 2004.

Vadas, S., Yue, J., and Nakamura, T.: Mesospheric concentric gravity waves generated by multiple convective storms over the North American Great Plain, Journal of Geophysical Research: Atmospheres, 117, D07 113, 2012.

Valladares, C. E. and Hei, M. A.: Measurement of the characteristics of TIDs using small and regional networks of GPS receivers during the campaign of 17–30 July of 2008, International Journal of Geophysics, 2012, 548 784, 2012.

VirginiaTech: Interactive Range-Time Plotting, `http://www.superdarn.com/tiki-index.php?page=DaViT+RTP`, [Online; accessed 2016/03/28], 2016.

Waldock, J. and Jones, T.: HF Doppler observations of medium-scale travelling ionospheric disturbances at mid-latitudes, Journal of atmospheric and terrestrial physics, 48, 245–260, 1986.

Walker, A. D. M.: Magnetohydrodynamic waves in geospace: the theory of ULF waves and their interaction with energetic particles in the solar-terrestrial environment, CRC Press, 2004.

Wang, Y., Zhang, Q.-H., Jayachandran, P., Lockwood, M., Zhang, S.-R., Moen, J., Xing, Z.-Y., Ma, Y.-Z., and Lester, M.: A comparison between large-scale irregularities and scintillations in the polar ionosphere, Geophysical Research Letters, 2016.

Weber, E., Klobuchar, J., Buchau, J., Carlson, H., Livingston, R., Beaujardiere, O., Mc-
Cready, M., Moore, J., and Bishop, G.: Polar cap F layer patches: Structure and dynamics,
Journal of Geophysical Research: Space Physics, 91, 12 121–12 129, 1986.

Yeoman, T. K., Chisham, G., Baddeley, L., Dhillon, R., Karhunen, T., Robinson, T., Senior,
A., and Wright, D.: Mapping ionospheric backscatter measured by the SuperDARN HF
radars – Part 2: Assessing SuperDARN virtual height models, Annales Geophysicae, 26,
843–852, 2008.

Yizengaw, E.: The Southern Hemisphere and equatorial region ionization response for a 22
September 1999 severe magnetic storm, Annales Geophysicae, 22, 1v7571, 2004.

Yizengaw, E., Dyson, P., Essex, E., and Moldwin, M.: Ionosphere dynamics over the South-
ern Hemisphere during the 31 March 2001 severe magnetic storm using multi-instrument
measurement data, Annales Geophysicae, 23, 519 487, 2005.

Zhang, Q.-H., Zhang, B.-C., Lockwood, M., Hu, H.-Q., Moen, J., Ruohoniemi, J. M.,
Thomas, E. G., Zhang, S.-R., Yang, H.-G., Liu, R.-Y., *et al.*: Direct observations of
the evolution of polar cap ionization patches, science, 339, 1597–1600, 2013.

Appendices

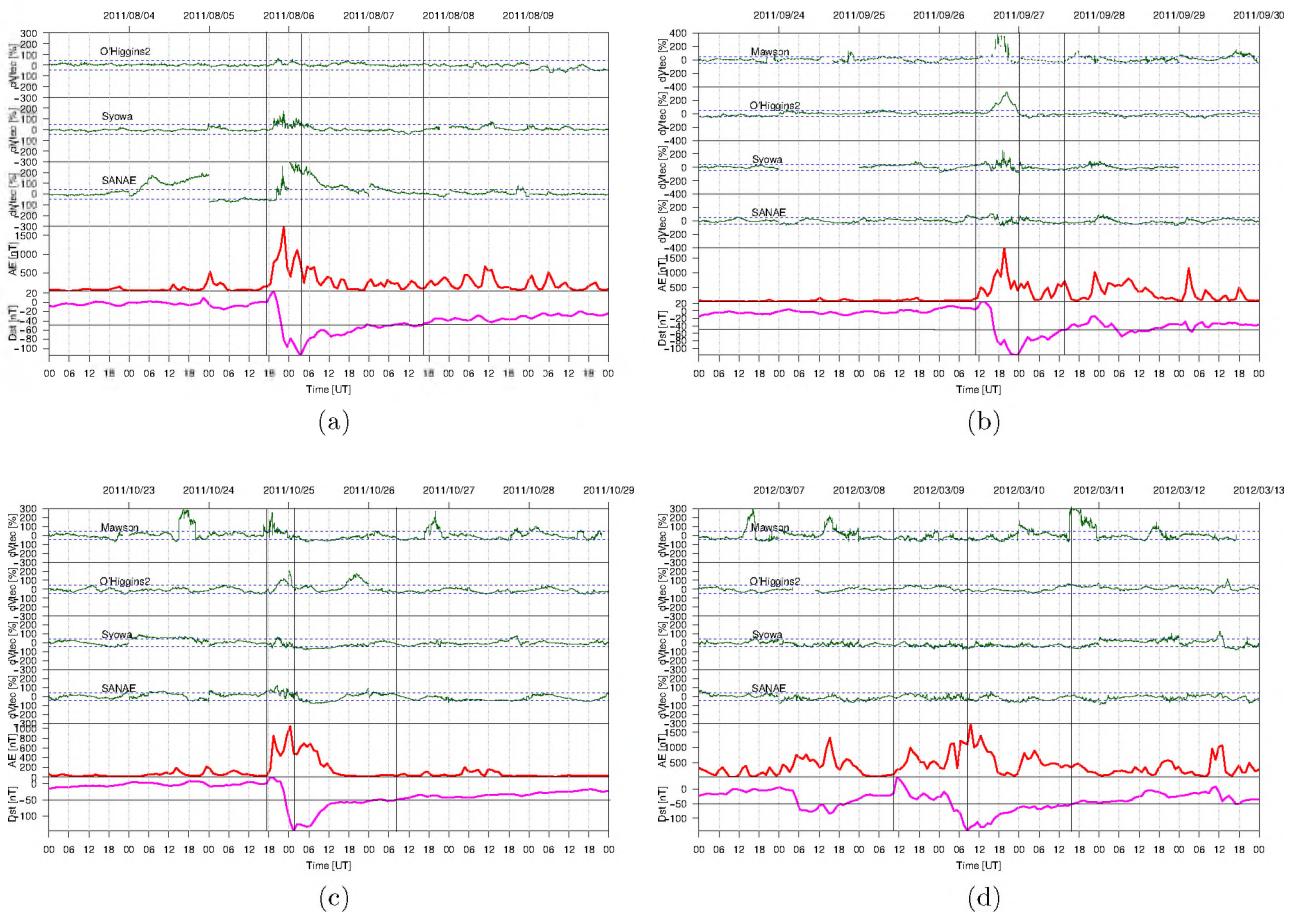# Appendix A

Figures of other storm effects

Figure A.1: The ionospheric storm effects for (a) 2011/08/06, (b) 2011/09/27, (c) 2011/10/25 and (d) 2012/03/09 storm days
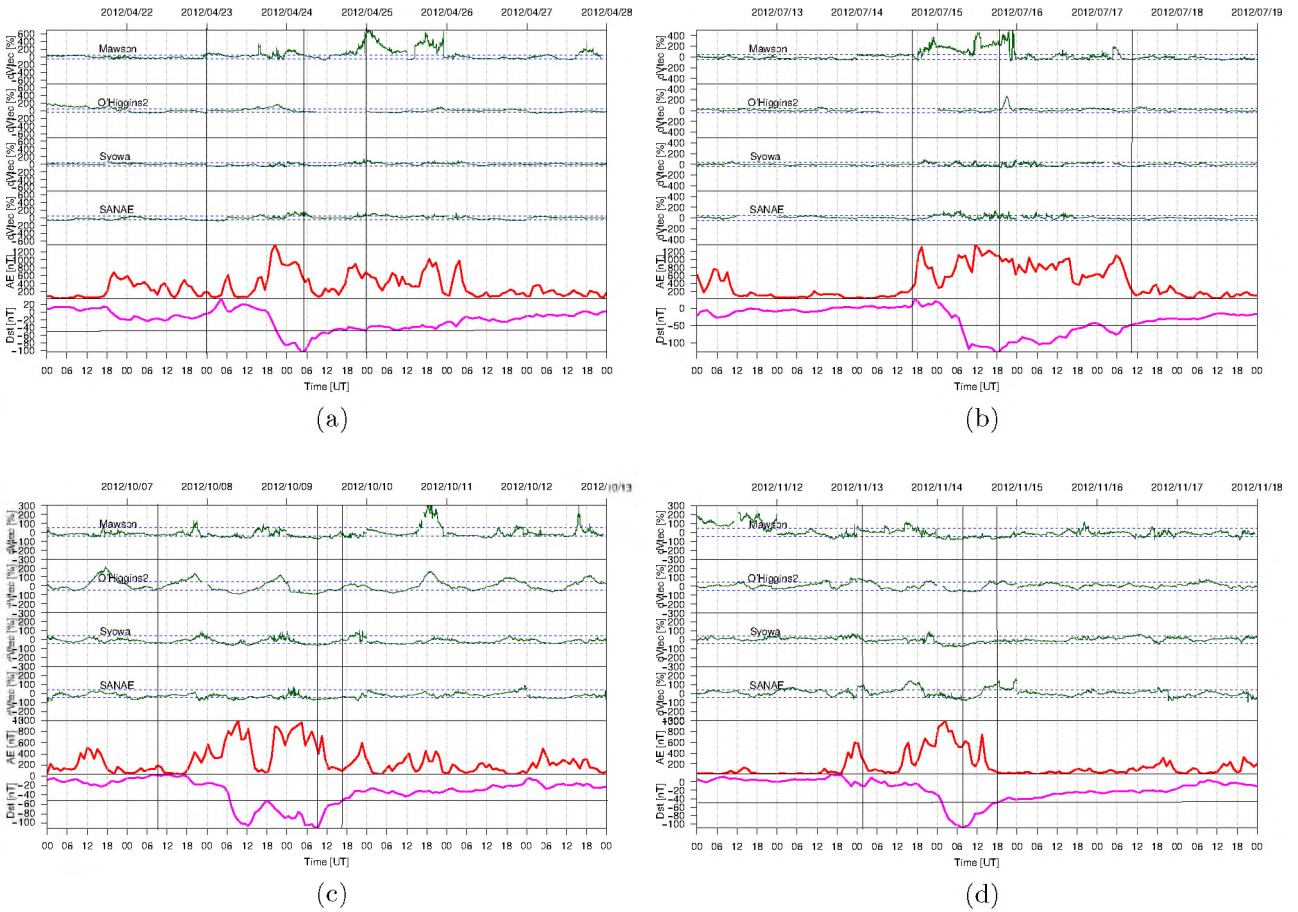
Figure A.2: The ionospheric storm effects for (a) 2012/04/24, (b) 2012/07/15, (c) 2012/10/09 and (d) 2012/11/14 storm days
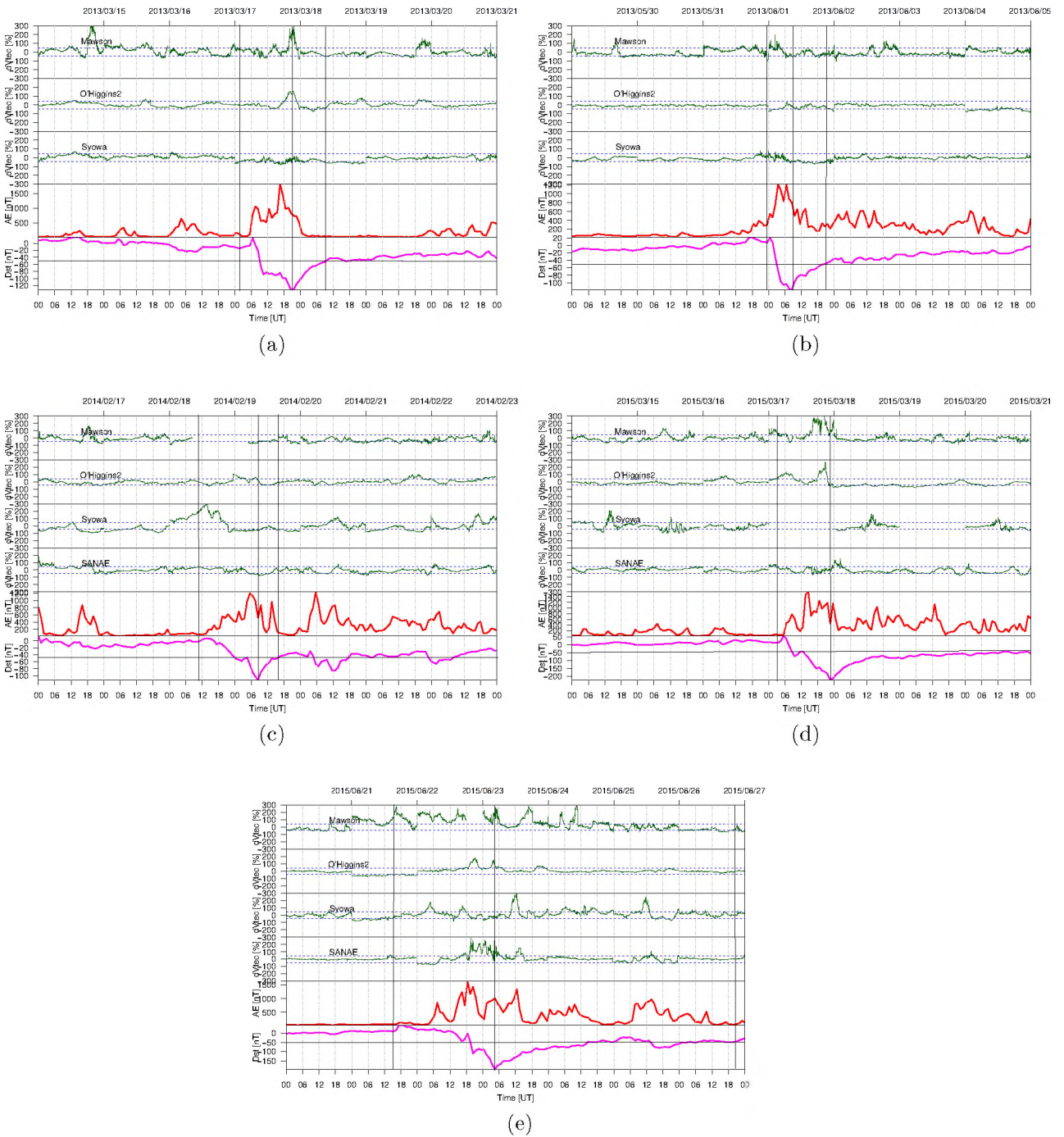
Figure A.3: The ionospheric storm effects for (a) 2013/03/17, (b) 2013/06/01, (c) 2014/02/19, (d) 2015/03/17 and (e) 2015/06/23 storm days

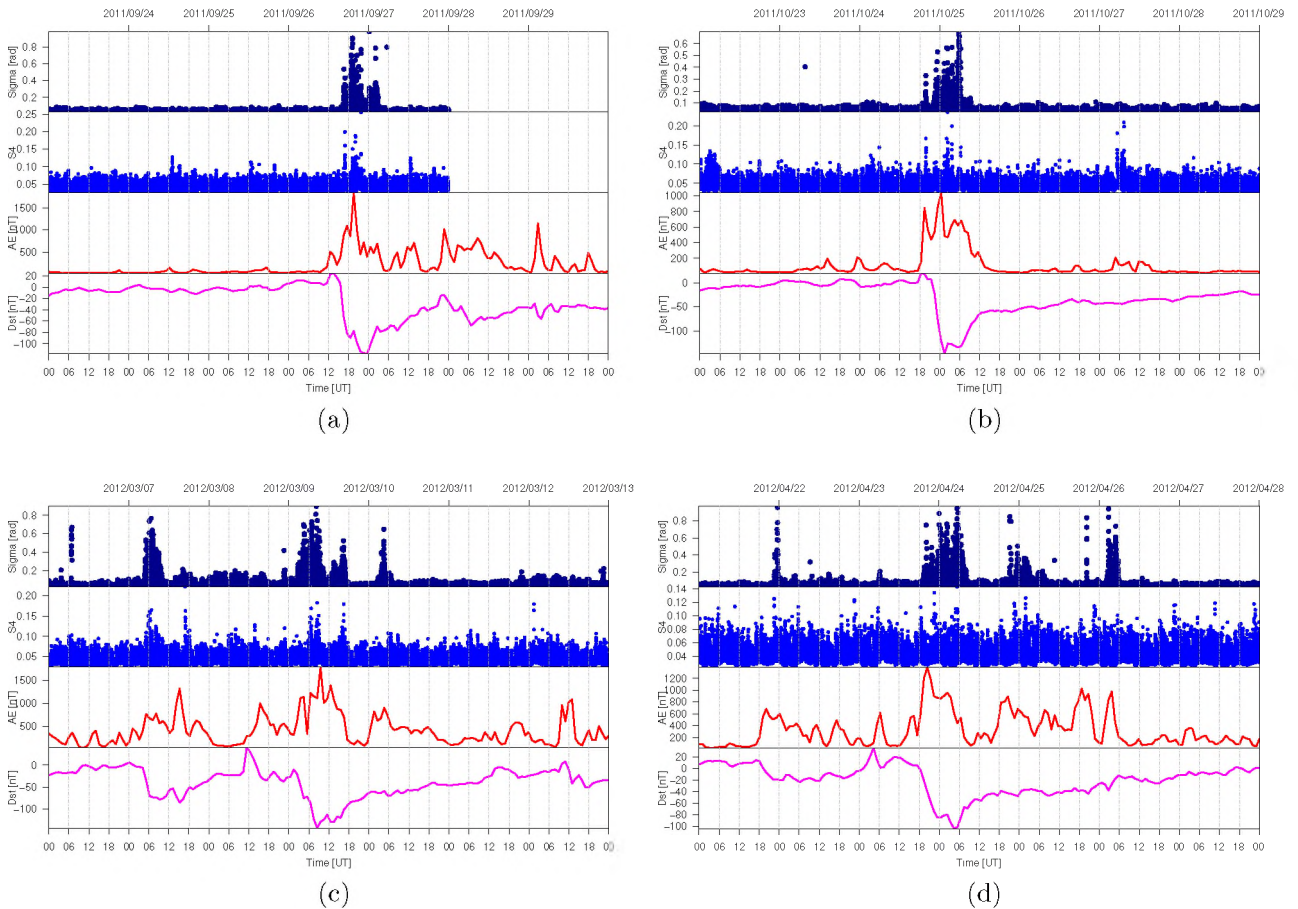# Appendix B

Figures of σ_ϕ and S_4 with Dst and AE indices

Figure B.1: The phase and amplitude scintillations for (a) 2011/09/27, (b) 2011/10/25, (c) 2012/03/09 and (d) 2012/04/24 storm days
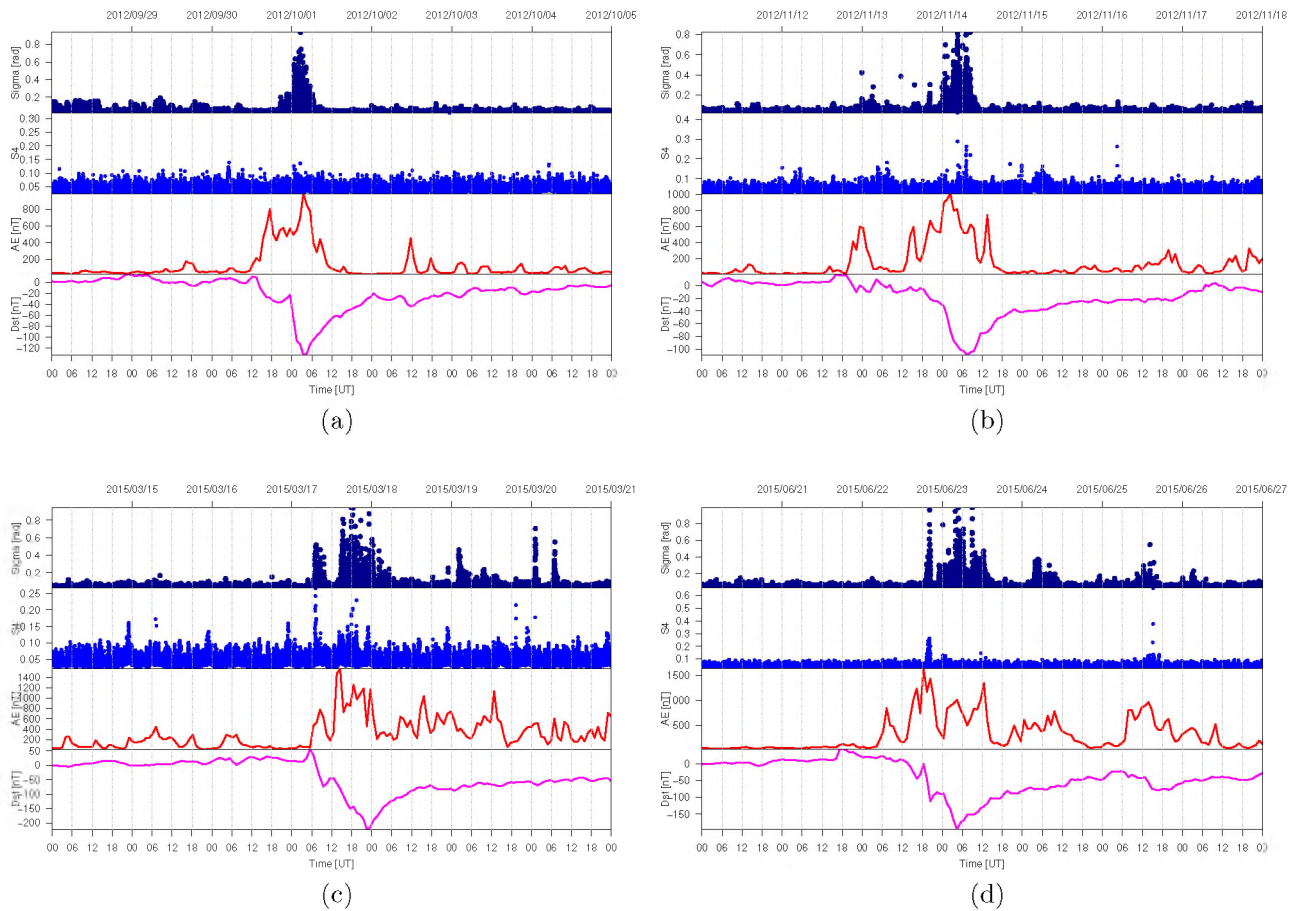
Figure B.2: The phase and amplitude scintillations for (a) 2012/10/01, (b) 2012/11/14, (c) 2015/03/17 and (d) 2015/06/23 storm days
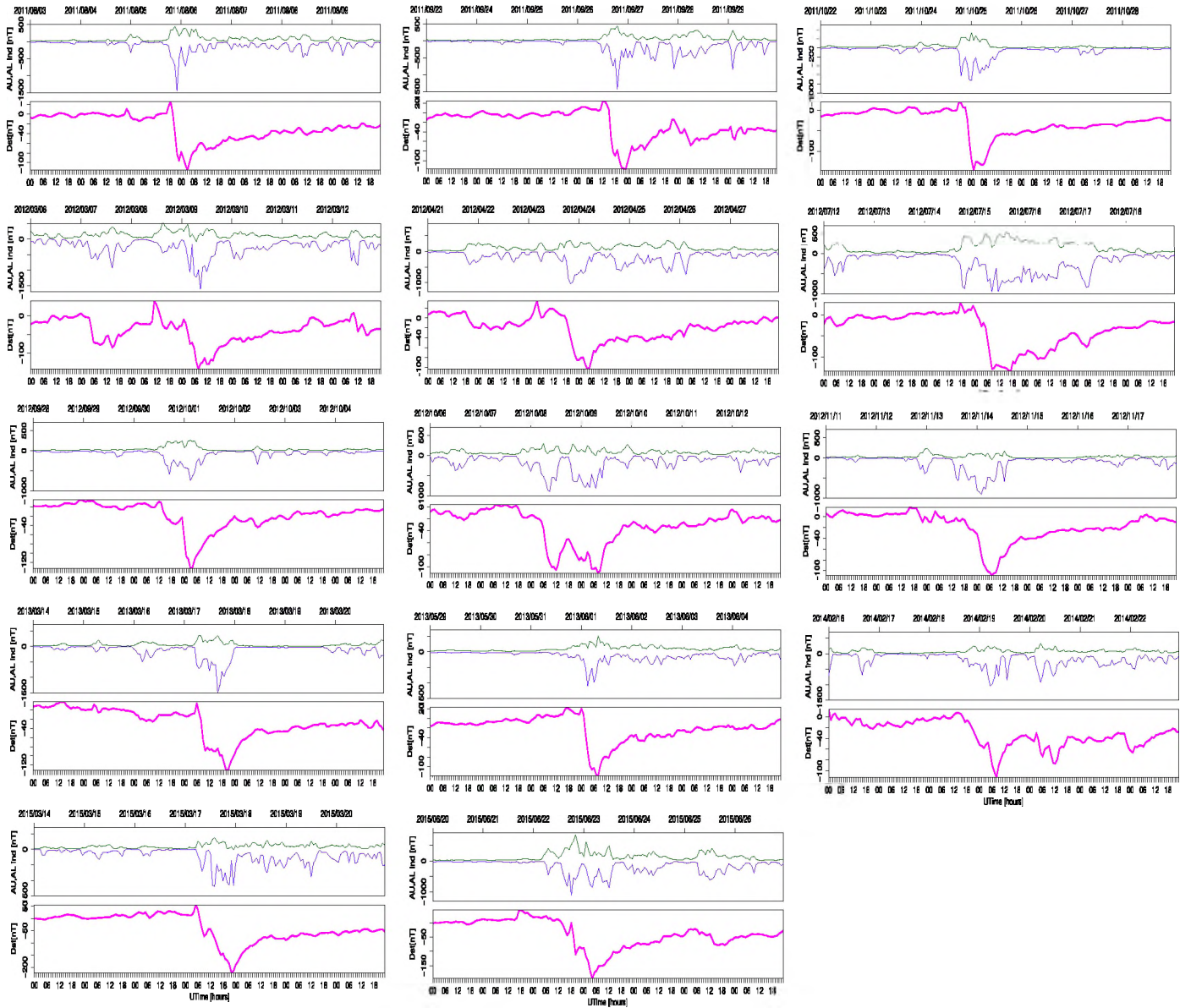
Appendix C

Plots of Dst, AU and AL indices

Figure C.1: The Dst, AU and AL indices of the storm days